

**CHARACTERIZATION AND FABRICATION OF
MULTIFUNCTIONAL GRADED DIELECTRICS
THROUGH ADDITIVE MANUFACTURING**

by

Austin J. Good

A thesis submitted to the Faculty of the University of Delaware in partial fulfillment of the requirements for the degree of Master of Science in Electrical and Computer Engineering

Spring 2016

© 2016
All Rights Reserved

ProQuest Number: 10156503

All rights reserved

INFORMATION TO ALL USERS

The quality of this reproduction is dependent upon the quality of the copy submitted.

In the unlikely event that the author did not send a complete manuscript and there are missing pages, these will be noted. Also, if material had to be removed, a note will indicate the deletion.



ProQuest 10156503

Published by ProQuest LLC (2016). Copyright of the Dissertation is held by the Author.

All rights reserved.

This work is protected against unauthorized copying under Title 17, United States Code
Microform Edition © ProQuest LLC.

ProQuest LLC.
789 East Eisenhower Parkway
P.O. Box 1346
Ann Arbor, MI 48106 - 1346

**CHARACTERIZATION AND FABRICATION OF
MULTIFUNCTIONAL GRADED DIELECTRICS
THROUGH ADDITIVE MANUFACTURING**

by

Austin J. Good

Approved: _____
Mark S. Mirotznik, Ph.D.
Professor in charge of thesis on behalf of the Advisory Committee

Approved: _____
Kenneth E. Barner, Ph.D.
Chair of the Department of Electrical and Computer Engineering

Approved: _____
Babatunde A. Ogunnaike, Ph.D.
Dean of the College of Engineering

Approved: _____
Ann L. Ardis, Ph.D.
Senior Vice Provost for Graduate and Professional Education

ACKNOWLEDGMENTS

I would like to thank my advisor, Dr. “Big Dog” Mirotznik, for his help and guidance for this work. I would also like to thank my peers: Matthew Mills, Peter Pa, Zachary Larimore, and Paul Parsons. Their assistance and advice made the research for my thesis a much smoother ride. I also would like to thank everyone in Dr. Mirotznik’s group for maintaining a fun and upbeat work environment; it made research a fun yet productive experience.

I would like to dedicate this work to my parents: Michael and Danette Good. I could not have asked for better parents. They have always been there for me during the stressful moments in my life. I am blessed to have their love and support.

TABLE OF CONTENTS

LIST OF TABLES	vi
LIST OF FIGURES	vii
ABSTRACT	xi

Chapter

1	INTRODUCTION	1
1.1	Contributions to Science.....	1
1.2	3D Powder Printer Introduction	2
1.3	Printer Overview	3
1.3.1	Printer GUI Manual	4
1.3.1.1	Powder Dispense Control	6
1.3.1.2	Motor Control	7
1.3.1.3	Printing Standard and Custom Printing Patterns	8
1.3.2	Printing Process	13
1.4	Materials Selection	16
2	CHARACTERIZATION OF COMBINED MATERIALS	18
2.1	Material Characterization	18
2.1.1	Out-of-Plane Characterization.....	18
2.1.2	In-Plane Characterization	19
3	ELECTROMAGNETIC APPLICATIONS USING DRY POWDER PRINTING	22
3.1	Microstrip Bragg Dielectric Reflector.....	22
3.1.1	Simulations and Design	23
3.1.2	Results	25
3.2	Chebyshev Antireflective Structure	26

3.2.1	Simulations and Design	26
3.2.2	Results	27
3.3	Cylindrical Luneburg Lens.....	30
3.3.1	Simulations and Design	31
3.3.2	Fabrication of Cylindrical Lens	42
3.3.3	Results	47
4	CONCLUSION	55
4.1	Summary of Work	55
4.2	Future Work.....	57
	REFERENCES	59

LIST OF TABLES

Table 1.1: Dielectric properties of materials used measured at 10 GHz.	17
Table 3.1: Designed and actual widths of dielectric sections	24
Table 3.2: Antireflective structure parameters	27

LIST OF FIGURES

Figure 1.1: Ultrasonic powder deposition system	4
Figure 1.2: Graphical User Interface (GUI) to control printing system	5
Figure 1.3: Powder dispense control section	6
Figure 1.4: Motor control section	7
Figure 1.5: Pattern input section	8
Figure 1.6: Populated Scatter Plot	9
Figure 1.7: Grid pattern	10
Figure 1.8: Hexagonal pattern	10
Figure 1.9: BMP to printing pattern	11
Figure 1.10: Move pipette to a certain point in “Scatter Plot”	12
Figure 1.11: 2D plot of dispensed powder locations	12
Figure 1.12: Close up of dispensing unit	14
Figure 1.13: Time lapse photographs of the powder printing dispensing tip	15
Figure 1.14: microCT image of a portion of a printed sample	15
Figure 1.15: Above is a timeline of the 3D printing process. a) powder is dispensed onto the composite substrate in a desired pattern, b) a IR heater softens the impregnated resin so the powder adheres to the substrate, c/d) all printed layers are aligned and stacked, e) an autoclave cures resin and binds stacked layers, and f) the end result is a robust part with embedded spatially varying dielectric properties.....	16
Figure 2.1: Example of a uniform print sample used to calibrate the transverse dielectric properties	19
Figure 2.2: Free-Space focused beam measurement system	19

Figure 2.3: Microstrip transmission line template.....	20
Figure 2.4: Fabricated transmission lines for calibration curve. Zoomed in images of powder spacing.	21
Figure 2.5: Calibration curves that relate in and out of plane permittivity to local powder density (mg/mm^2).....	21
Figure 3.1: Plot of the ideal reflection response.....	22
Figure 3.2: Simulated results of Bragg reflector	23
Figure 3.3: Fabricated Bragg dielectric reflector transmission line	24
Figure 3.4: Reflection response of measured and simulated results.....	25
Figure 3.5: Antireflective structure response	26
Figure 3.6: Antireflective template.....	27
Figure 3.7: Fabricated baseline transmission lines.....	28
Figure 3.8: Fabricated baseline reflection response	28
Figure 3.9: Fabricated antireflective transmission line	29
Figure 3.10: Fabricated antireflective reflection response	29
Figure 3.11: Luneburg lens excitation and output [19]	30
Figure 3.12: Standard Luneburg lens dielectric constant distribution.....	32
Figure 3.13: Scaled Luneburg lens relative dielectric constant distribution	33
Figure 3.14: Modified Luneburg lens relative dielectric constant distribution	34
Figure 3.15: HFSS model of cylindrical Luneburg lens.....	35
Figure 3.16: HFSS model of cylindrical Luneburg lens with annotated dielectric distribution.....	35
Figure 3.17: System without dielectric gradient.....	36
Figure 3.18: Electric field color map of -30 degree input	37
Figure 3.19: Unwrapped normalized phase using the -30 degree input	37

Figure 3.20: Electric field color map of -15 degree input	38
Figure 3.21: Normalized unwrapped phase using the -15 degree input	38
Figure 3.22: Electric field color map of 0 degree input.....	39
Figure 3.23: Normalized unwrapped phase using the 0 degree input	39
Figure 3.24: Electric field color map of +15 degree input	40
Figure 3.25: Normalized unwrapped phase using the +15 degree input	40
Figure 3.26: Electric Field color map of +30 degree input	41
Figure 3.27: Normalized unwrapped phase using the +30 degree input	41
Figure 3.28: MATLAB figure of dot distribution exported to the 3D powder printer.	43
Figure 3.29: Printed substrate.....	44
Figure 3.30: Printed and cut substrate	44
Figure 3.31: Cut ground plane.....	45
Figure 3.32: CAD file used for patterning top conductor	45
Figure 3.33: SMA connector and terminating load (images acquired from Digi- Key) [26-27]	46
Figure 3.34: Fabricated part	47
Figure 3.35: Reflection	48
Figure 3.36: Transmission	48
Figure 3.37: Input/output configuration for measurements.....	49
Figure 3.38: -30 degree input	51
Figure 3.39: -15 degree input	51
Figure 3.40: 0 degree input.....	52
Figure 3.41: +15 degree input	52
Figure 3.42: +30 degree input	53

Figure 4.1 : nScript's 3Dn-300 additive manufacturing system [28]	58
---	----

ABSTRACT

The ability to fabricate multifunctional devices that combine good structural properties with embedded electromagnetic functionality has many practical applications. These include, but are not limited to, antireflective surfaces for structural radomes, load bearing conformal antennas, integrated RF transmission lines, and passive beam forming networks.

A custom made 3D printer, made here at the University of Delaware, is capable of printing high dielectric constant ceramic powders within a low-loss structural composite substrate resulting in mechanically robust parts with integrated graded dielectric properties. The first part of my thesis will evaluate the anisotropic dielectric properties that result from powder printing. A number of samples were fabricated and used to determine the complete permittivity tensor of the printed samples as a function of local powder weight. The remainder of the thesis will explain the designed and built systems that utilize the permittivity tensor. The results of these systems will demonstrate the accuracy of the established permittivity tensor and show the effectiveness of 3D powder printing.

Chapter 1

INTRODUCTION

1.1 Contributions to Science

During my time at the University of Delaware, I have had the opportunity to attend one international conference and work on two academic journals. The international conference was IEEE's International Symposium on Antennas and Propagation and North American Radio Science Meeting. The conference took place in Vancouver, Canada on July 19-24, 2015. I participated in the conference by giving a 20 minute presentation on my most up to date research and competing in the Student Paper Competition. For the Student Paper Competition, 173 graduate students across the world submitted a 2 page summary of their research. Of those 173 graduate students, 13 finalists were chosen to give a poster presentation on their research to the whole conference and judges. Awards were given to the top three average scores given by the judges. I received first place. The 20 minute presentation took place during the Novel Materials and Conductive Inks for Additive Manufacturing of Antennas session of the conference. My talk was titled "In-Plane Characterization of Graded Dielectrics Fabricated Through Additive Manufacturing". My talk consisted of Chapters 1, 2, 3.1, and 3.2 of this thesis.

One of the two academic journals has been completed and submitted to IEEE's Transactions on Microwave Theory and Techniques. The paper is titled "Multifunctional Graded Dielectrics Fabricated using Dry Powder Printing." It is currently being considered for publication. I am currently working on the second of

the two academic journal. The writing portion has made little progress, however the research has been completed. This journal will describe the passive beamforming network found in Chapter 3.3. The goal is to have both papers submitted and accepted for publication before the date of graduation.

1.2 3D Powder Printer Introduction

The ability to control electromagnetic wave propagation using a spatially varying or graded index of refraction (GRIN) is utilized in a number of practical photonic devices (e.g. GRIN lenses and graded index optical fibers). At microwave frequencies, GRIN structures have been explored for use as lens antennas [1], antireflective surfaces [2] and passive beam formers [3]. However, fabricating practical GRIN structures at microwave frequencies can be challenging. One popular technique is subtractive manufacturing. This method utilizes computer numerical control (CNC) milling to create spatially varying air voids within a solid homogenous dielectric. Assuming the void size and spacing is much smaller than the wavelength, the combination of air pockets and background create a locally varying effective permittivity. Unfortunately, for many applications drilling air pockets into a substrate significantly compromises the structural integrity of the device.

To fabricate a mechanically robust sample, it is much more attractive to employ additive manufacturing methods. To this end, we have designed and built a 3D printer that dispenses dry high permittivity powders between layers of a structural composite to create graded dielectrics [4]. It was shown in [4] that this approach has only a small effect on the mechanical strength of the structural composite. One consequence of this fabrication process is that the resulting permittivity distribution is anisotropic with different values in the xy-plane (i.e. transverse plane) and along the z-

axis (i.e. longitudinal axis). In this study, I extend the previous studies by examining the full permittivity tensor resulting from this additive manufacturing process and validate those properties using three illustrative examples. I also provide an effective media model that can be used to predict the anisotropic properties as a function of materials and print parameters.

1.3 Printer Overview

A custom 3D powder printer, illustrated in Figure 1.1, was developed to create multifunctional structures with integrated electromagnetic properties. The dielectric properties are manipulated by dispensing a high permittivity powder (Emerson & Cuming's HiK) [5] onto a low-loss woven fabric based composite material (BTCy-1 6781 by TenCate) [6]. A spatially varying powder distribution is realized by moving an electrically controlled power valve over the surface of the composite substrate. At any specific location the ratio of dispensed powder to surface area defines the local effective permittivity.

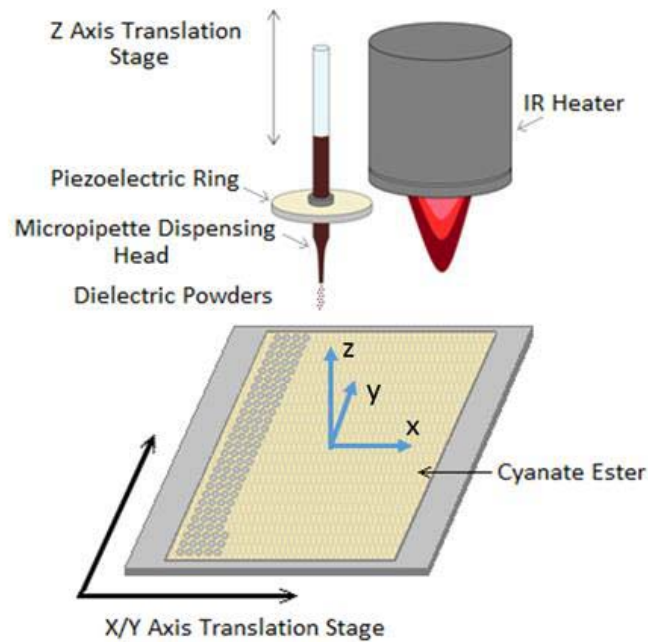


Figure 1.1: Ultrasonic powder deposition system

1.3.1 Printer GUI Manual

In order to computerize the printing process, a custom-made graphical user interface (GUI) was created. This GUI has the ability to move the printing platform in the X and Y directions, zero the rotational stage, toggle powder deposition, load custom 2D designs to be printed (hexagonal/grid patterns as well as images with varying patterns), and pause/resume custom 2D designs. This allows the user to interact with multiple different machines through the simplicity of one single interface.

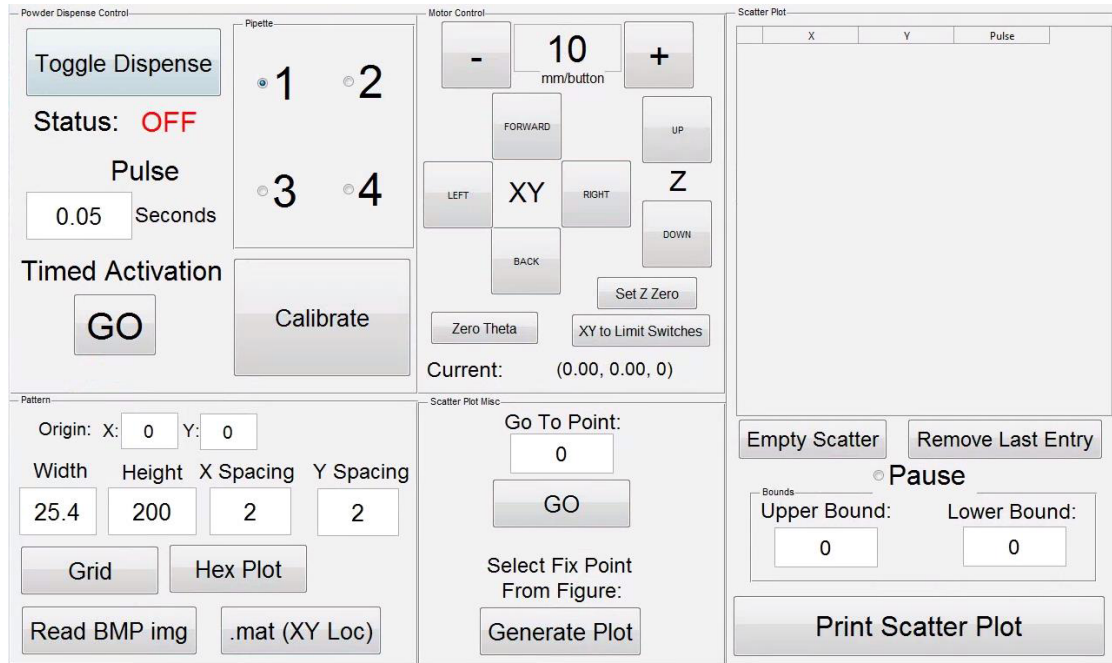


Figure 1.2: Graphical User Interface (GUI) to control printing system

Figure 1.2 is a screenshot of the entire GUI. The GUI was programmed in MATLAB. The GUI is broken down into five unique sections: powder dispense control, patterns, motor controls, jog to location, and scatterplot overview. The remainder of Chapter 1.2 will explain how each section of the GUI works.

1.3.1.1 Powder Dispense Control

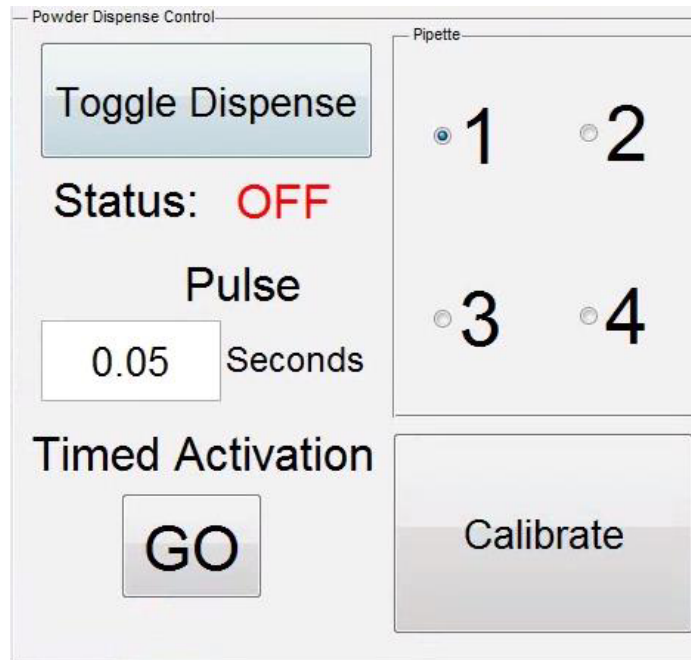


Figure 1.3: Powder dispense control section

This section of the GUI focuses on powder deposition control. This section serves four purposes. First, “Toggle Dispense” will begin powder flow in a functioning pipette. The button will toggle on/off the function generator to vibrate the piezoelectric ring. Second, the “Timed Activation” function will toggle on the function generator to vibrate the pipette for a desired duration of time. This can be utilized to dispense where a programmed print patterned failed to place powder (this happens on occasion). Third, the radio button “Pipette” window allows you to mount multiple pipettes to the printer to print multiple materials at once. Lastly, the “Calibrate” function will deliver 100 timed pulses of the time listed under the “Pulse” heading. This will allow you to figure out how many milligrams of powder are being dispensed

per pulse. The user can do this by placing a scale underneath the tip of the pipette and measure how many milligrams are dispensed at the conclusion of 100 pulses. Take the total weight and divide it by 100. The resulting number describes how many milligrams are dispensed per pulse.

1.3.1.2 Motor Control

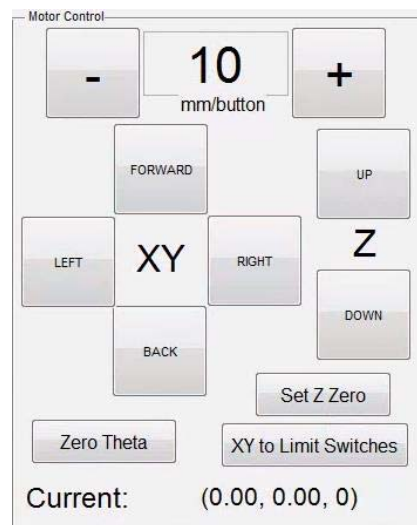
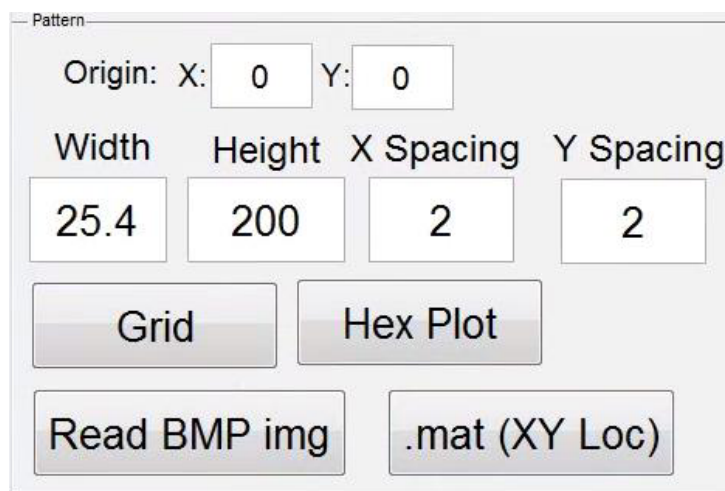


Figure 1.4: Motor control section

The “Motor Control” section of the GUI allows the user to move the height of the pipette and the stage that holds the printing substrate. It serves the role of positioning the origin of printing patterns. The user will position the pipette head above the bottom left location of the desired pattern. I will go into more detail regarding this in the “Pattern” section.

1.3.1.3 Printing Standard and Custom Printing Patterns



The image shows a GUI window titled "Pattern". It contains several input fields and buttons. At the top, there are two input fields for "Origin: X:" and "Y:", both containing the value "0". Below these are four input fields for "Width", "Height", "X Spacing", and "Y Spacing", containing the values "25.4", "200", "2", and "2" respectively. At the bottom, there are four buttons: "Grid", "Hex Plot", "Read BMP img", and ".mat (XY Loc)".

Figure 1.5: Pattern input section

The “Pattern” section of the GUI allows the user to program the printer to dispense powder in two standard patterns (grid and hexagonal) and any custom pattern (using a BMP image or a matrix of locations). To place the origin for these patterns, position the pipette above the origin location as shown in Figure 1.7 and Figure 1.8. Once these patterns are executed, the locations of each pulse will populate in the “Scatter Plot” table as show in Figure 1.6.

Scatter Plot			
	X	Y	Pulse
1	250	-250	0.0500
2	252	-250	0.0500
3	254	-250	0.0500
4	256	-250	0.0500
5	258	-250	0.0500
6	260	-250	0.0500
7	262	-250	0.0500
8	264	-250	0.0500
9	266	-250	0.0500
10	268	-250	0.0500
11	270	-250	0.0500
12	272	-250	0.0500
13	274	-250	0.0500
14	251	-248.2679	0.0500
15	253	-248.2679	0.0500
16	255	-248.2679	0.0500

Figure 1.6: Populated Scatter Plot

Figures 1.7 and 1.8 demonstrate how the dots will be arranged when using the grid and hexagonal patterns. For the grid pattern, the spacing of dots in the X and Y directions can be controlled by changing the values in the “X Spacing” and “Y Spacing” edit boxes.

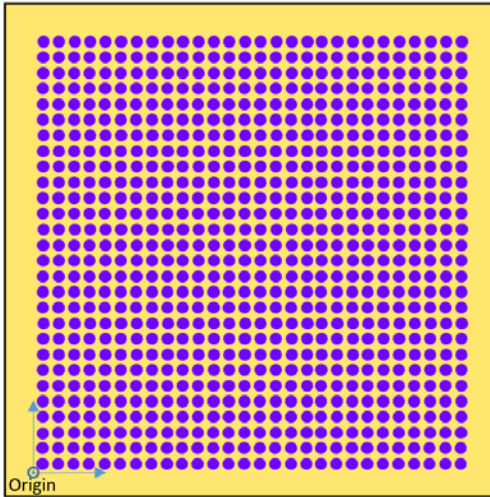


Figure 1.7: Grid pattern

For the hexagonal pattern, only the “X Spacing” value will be used. The pattern uses only equilateral triangles. If you enter a value for “X Spacing” and press Hex Plot, the edit box for Y Spacing will update with the value: $\frac{\text{X Spacing}}{2} \times \sqrt{3}$.

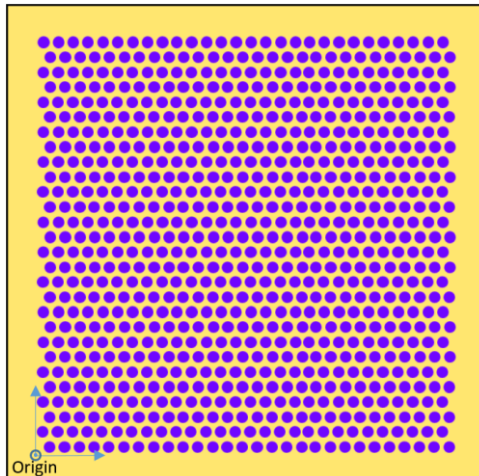


Figure 1.8: Hexagonal pattern

“Read BMP img” and “.mat (XY Loc)” functionalities are mostly for demonstration purposes. For example, to showcase the printer to guests and sponsors, the UD logo was printed. The UD.bmp, shown in Figure 1.9, is read pixel by pixel and will generate a printing pattern. This pattern will be populated in the “Scatter Plot” section and will be ready to print at will.

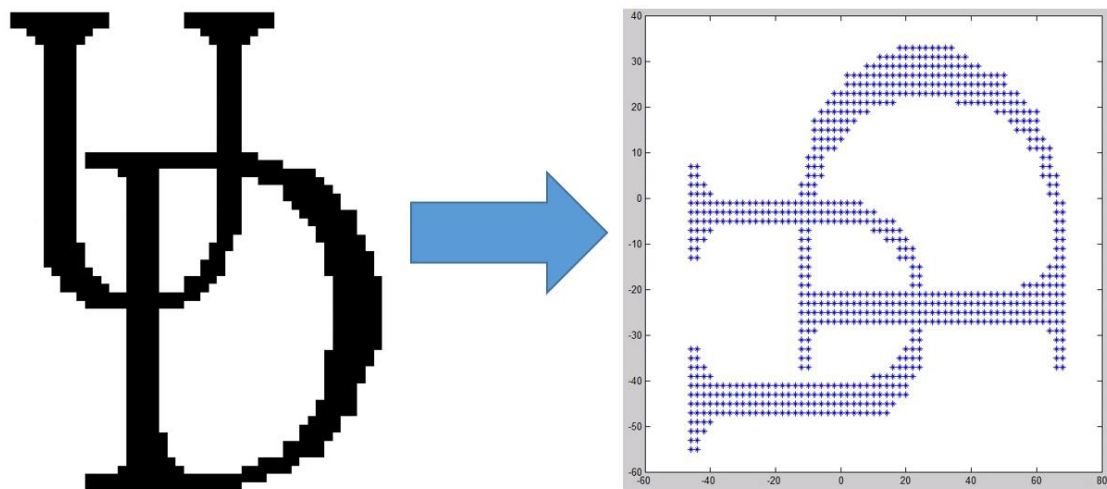


Figure 1.9: BMP to printing pattern

Once a printing pattern is loaded in the “Scatter Plot” table, the user has a variety of options at this point. The user can immediately begin printing, verify that the pattern will fit on the given substrate, or adjust the starting/end locations. The next two figures and paragraphs will explain how the user can achieve this.

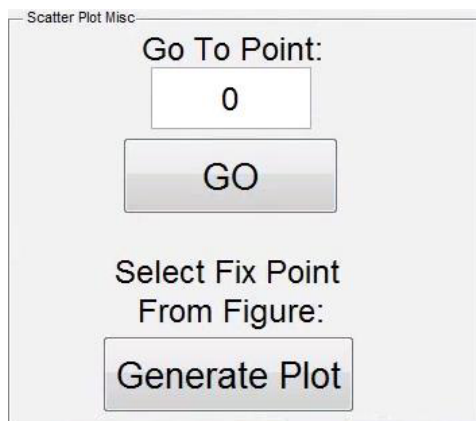


Figure 1.10: Move pipette to a certain point in “Scatter Plot”

Figure 1.10 allows the user to jog a certain location populated in the “Scatter Plot” table. This is achieved by entering a value in the “Go To Point:” edit text box. The entered value corresponds with the numbered row in the “Scatter Plot” table. If the user presses “Generate Plot”, a figure will come into focus displaying the dot locations in a 2D plot (Figure 1.11).

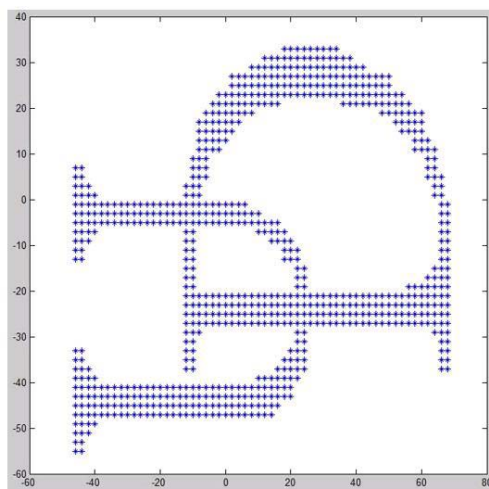


Figure 1.11: 2D plot of dispensed powder locations

Once the user is ready to begin printing, you need jog to location 1 of the pattern before printing. Now the user is ready to print. Press “Print Scatter Plot” to begin printing. If the printing process encounters any issues, press the “Pause” radio button. You can now jog to previous locations to fill in any missed dots. If more intensive intervention is needed, press Ctrl + C in the MATLAB command window to kill the whole printing process.

1.3.2 Printing Process

In order to dispense the dry powder in a desired pattern, a “valve” based deposition system was used (see Figure 1.12). The design of this dispensing system, composed of a glass pipette and bonded piezoelectric ring, was originally described by Yang et. al. [7-14]. The diameter of the pipette opening is small enough such that powder does not dispense under static conditions. Specifically, this requires the pipette orifice to be approximately 5 to 6 particle diameters at its tip. To initiate powder flow, a piezoelectric ring is vibrated at 42 kHz. Figure 1.13 shows time-lapse photographs of the powder being dispensed. The powder that flows out of the pipette will land on the substrate and form a small dot. The amount of powder dispensed depends on size of the pipette orifice and the duration of the 42 kHz pulse. The average powder dot size typically used is 2-2.5 mm in diameter. This is equivalent to approximately 2 milligrams of powder.

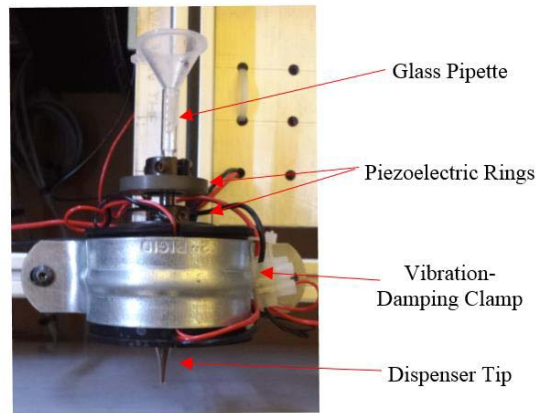


Figure 1.12: Close up of dispensing unit

After each layer is printed an infrared heater is scanned over the surface to slightly heat the substrate. This causes the resin to become tacky resulting in good powder adhesion. To achieve spatially varying permittivity in three dimensions the printed layers are aligned and stacked prior to post-processing in an autoclave. The autoclave is needed to cure the impregnated resin, bind stacking substrates together, and remove unwanted air pockets. The final result is a structurally robust plate with integrated dielectric properties. Figure 1.15 provides a visual overview of the entire process. The final part is a mechanically robust structure with the spatially varying powder distribution permanently integrated. Figure 1.14 shows a micro-CT scan of a small portion of a sample after post-processing. This sample was composed of eight printed and stacked layers. This image illustrates how the powder distributes itself between substrate layers. It is evident by examining the symmetry of the final part that the dielectric properties are likely to be anisotropic with different properties in the transverse xy-plane than the longitudinal z-axis.

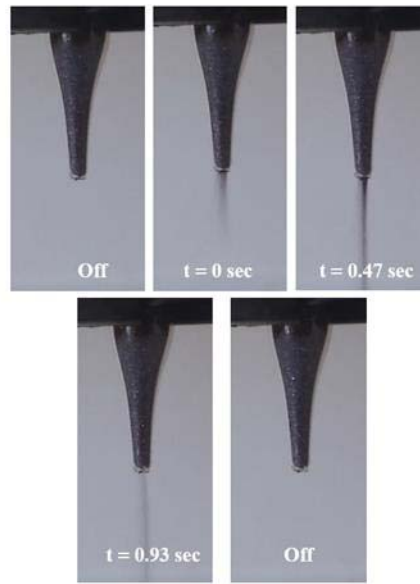


Figure 1.13: Time lapse photographs of the powder printing dispensing tip

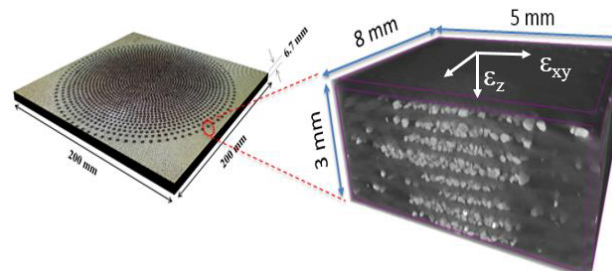


Figure 1.14: microCT image of a portion of a printed sample

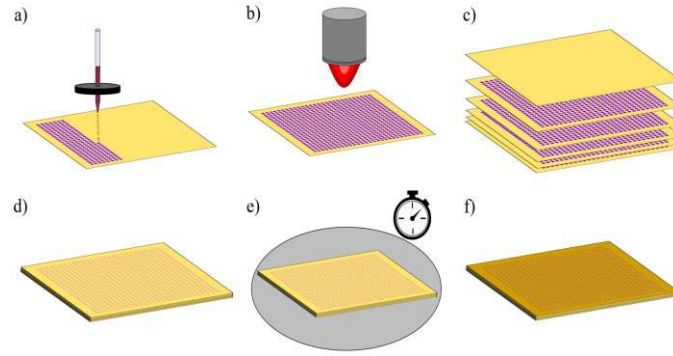


Figure 1.15: Above is a timeline of the 3D printing process. a) powder is dispensed onto the composite substrate in a desired pattern, b) a IR heater softens the impregnated resin so the powder adheres to the substrate, c/d) all printed layers are aligned and stacked, e) an autoclave cures resin and binds stacked layers, and f) the end result is a robust part with embedded spatially varying dielectric properties

1.4 Materials Selection

There were three main criteria taken into consideration for selecting materials for this system. Namely, mechanical resiliency, low loss tangent, and high dielectric constant contrast between dispensed powder and substrate.

The substrate that was chosen was an S-glass/cyanate ester fiber reinforced composite prepreg (BTCy-1 sold by TenCate). Further details regarding these materials can be found at the links found in the references [5-6] and [15]. This material has desirable mechanical properties and a low microwave loss tangent.

Table 1.1: Dielectric properties of materials used measured at 10 GHz.

Material	Dielectric Constant	Loss Tangent
BTCy-1 Composite Substrate	4.2	0.003
Emerson & Cuming's HiK Powder	12.0	0.0007

ECCOSTOCK® HiK Powder was selected as the dispensed material. The HiK ceramic powder was chosen due to its relatively high dielectric constant, low loss tangent, and large particle sizes ($\sim 100\ \mu\text{m}$). The large particle sizes are well suited for the powder dispensing apparatus discussed previously.

Chapter 2

CHARACTERIZATION OF COMBINED MATERIALS

2.1 Material Characterization

To determine a relationship between the quantity of powder deposited per unit area and the effective permittivity tensor, described by Equation (1), a number of calibration samples were fabricated.

$$\bar{\bar{\epsilon}}_{eff} = \begin{bmatrix} \epsilon_{xy} & 0 & 0 \\ 0 & \epsilon_{xy} & 0 \\ 0 & 0 & \epsilon_z \end{bmatrix} \quad (1)$$

To determine both the transverse (i.e. ϵ_{xy}) and longitudinal (i.e. ϵ_z) components of the permittivity tensor I performed two sets of calibration experiments.

2.1.1 Out-of-Plane Characterization

For the calibration of the transverse components, eight samples of varying powder densities, 0 mg/mm² to 0.51 mg/mm², were fabricated (an example is shown in Figure 2.1). Each sample was a 300 mm x 300 mm x 3 mm uniform plate in which the dot-to-dot spacing was varied while maintain a consistent powder dot weight. To determine the transverse effective permittivity values (i.e. ϵ_x and ϵ_y) of each sample, a focused beam material measurement system, described in [4], was used (Figure 2.2). Over the range of frequencies tested (i.e. 4 GHz to 18 GHz) the maximum dot-to-dot spacing did not exceed 5 mm. This ensured that even at the highest frequency tested the dot spacing was smaller than the wavelength ($\lambda/3$) and could be treated as an

effective permittivity. Results from the eight samples were then combined to establish a calibration curve (Figure 2.2).

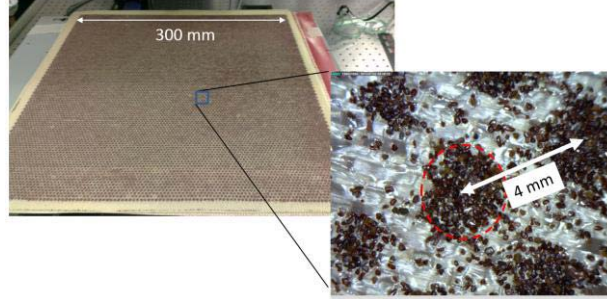


Figure 2.1: Example of a uniform print sample used to calibrate the transverse dielectric properties

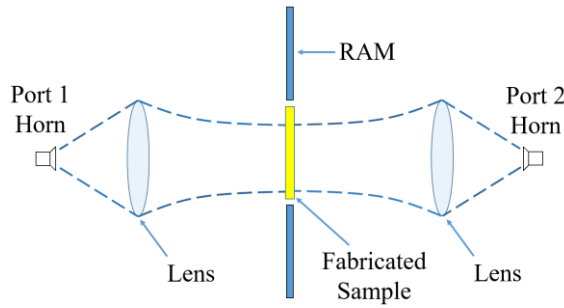


Figure 2.2: Free-Space focused beam measurement system

2.1.2 In-Plane Characterization

To determine the longitudinal component (i.e. ϵ_z), a microstrip transmission line method was utilized. For this test, seven samples were fabricated with local powder densities that varied from 0 mg/mm² to 0.66 mg/mm² (Figure 2.4). An Agilent E8364 PNA was used to measure the complex transmission coefficient, S₂₁, over the frequency band of interest. The effective permittivity of the powder printed substrate,

$\epsilon_{\text{substrate}}$, was then calculated from the measured effective permittivity of the fundamental microstrip mode, ϵ_{eff} , using the quasi-static approximation [16] given by

$$\epsilon_{\text{eff}} = \frac{\epsilon_r + 1}{2} + \frac{\epsilon_r - 1}{2} \frac{1}{\sqrt{1 + 12d/W}} \quad (2)$$

$$\epsilon_{\text{substrate}} = \frac{1 + (2\epsilon_{\text{eff}} - 1) \sqrt{1 + 12\left(\frac{d}{W}\right)}}{1 + \sqrt{1 + 12\left(\frac{d}{W}\right)}} \quad (3)$$

where h is the substrate thickness and W is the width of the metallic microstrip trace. The effective permittivity was directly back out of measurements using

$$\epsilon_{\text{eff}} = \left(\frac{\partial \phi}{df} \cdot \frac{2}{2\pi l} \right)^2 \quad (4)$$

where, l is the length of the transmission lines, c is the speed of light in vacuum and $d\phi/df$ denotes the rate of change of transmitted phase with respect to frequency.

After measurement and data processing, I arrived at the set of calibration curves, shown in Figure 2.5, that predict the local effective permittivity tensor of the printed samples as a function of the amount of powder dispensed.

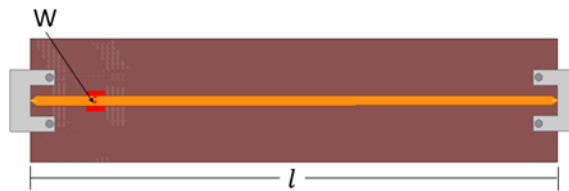


Figure 2.3: Microstrip transmission line template

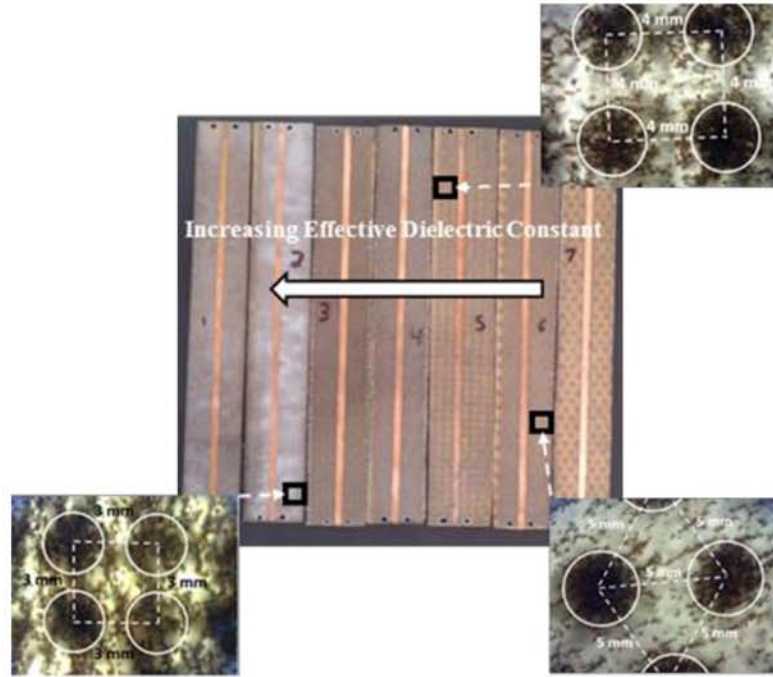


Figure 2.4: Fabricated transmission lines for calibration curve. Zoomed in images of powder spacing.

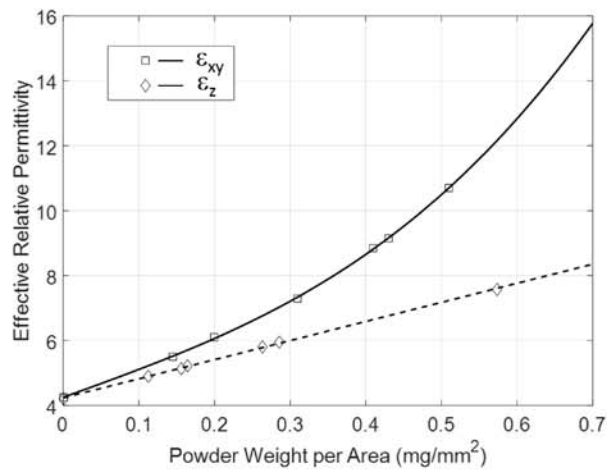


Figure 2.5: Calibration curves that relate in and out of plane permittivity to local powder density (mg/mm²)

Chapter 3

ELECTROMAGNETIC APPLICATIONS USING DRY POWDER PRINTING

3.1 Microstrip Bragg Dielectric Reflector

To validate the calibration data shown above, I designed and fabricated the simple Bragg based guided mode filter [17]. Reference 17 describes the Bragg reflector as multiple layers of dielectric materials. Here, I am trying to create the same concept of multiple layers but through microstrip transmission lines [18]. The length of each of the sections of low and high permittivity were designed to be a quarter wavelength in the material as given by

$$l_{low/high} = \frac{c}{4f_c \sqrt{\epsilon_{low/high}}} \quad (5)$$

This creates a Bragg condition resulting in a highly reflective mirror centered at the frequency, f_c (Figure 3.1).

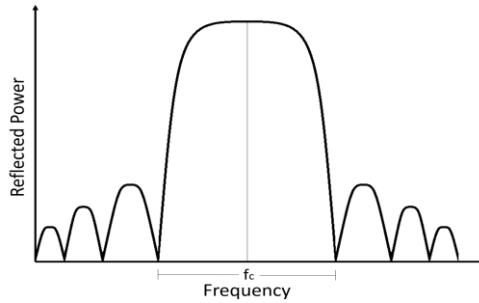


Figure 3.1: Plot of the ideal reflection response

3.1.1 Simulations and Design

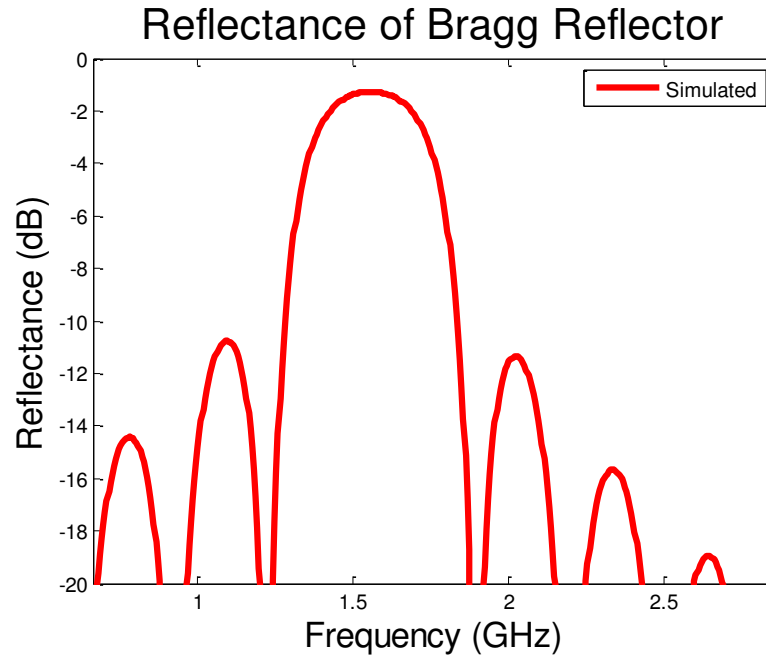


Figure 3.2: Simulated results of Bragg reflector

For this example, the powder printer was used to fabricate a mechanically rigid substrate ($263 \times 75 \times \sim 1.2\text{-}1.7$ mm) with alternating sections of low and high permittivity (shown in Figure 3.3). A copper ground plane and microstrip trace were then attached to the bottom and top surfaces of the printed substrate respectively.

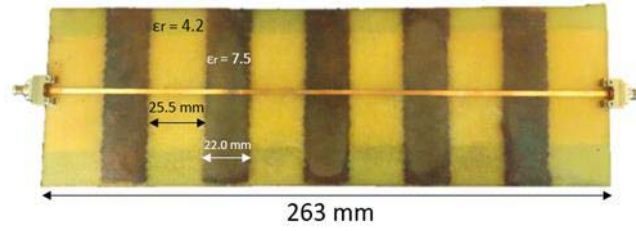


Figure 3.3: Fabricated Bragg dielectric reflector transmission line

Table 3.1: Designed and actual widths of dielectric sections

	Desired	Actual
Low Dielectric Length	28.2 mm	25.5 mm
High Dielectric Length	21.9 mm	22.0 mm

For this test sample, I selected high and low relative permittivities of $\epsilon_{\text{High}} = 7.5$ and $\epsilon_{\text{Low}} = 4.2$ respectively. The substrate thickness varies between 1.2 mm and 1.7 mm (substrate height varies due to added powder) and the microstrip trace width was chosen to be $W=2.0$ mm. This results in a 50Ω characteristic impedance at the connectors. The length of the high and low sections were then determined by Equation (5) to be $l_{\text{Low}}=28.2$ mm and $l_{\text{High}} = 21.9$ mm respectively.

The Bragg based transmission line filter was then fabricated using the powder printer described previously. Figure 3.3 shows the fabricated sample. The measured reflectance from the transmission line is shown in Figure 3.4. Figure 3.3 shows the simulated results using a MATLAB multilayered lab script. Each subsection (high/low section) is modeled using the calculated effective relative permittivity.

3.1.2 Results

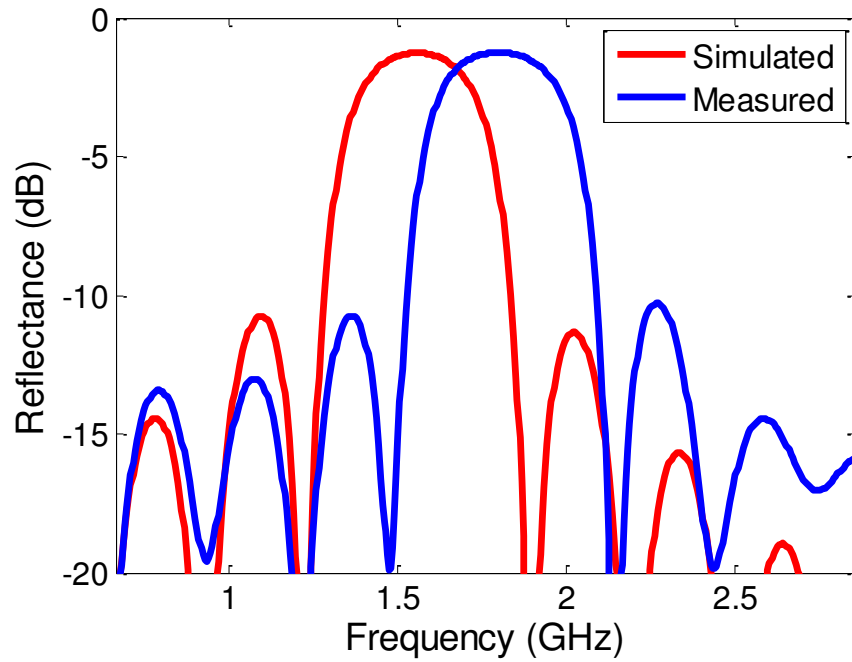


Figure 3.4: Reflection response of measured and simulated results

The measured results differ in peak reflection as well as center frequency when compared to the simulated design. The measured peak reflectance is slightly shifted towards a higher frequency (~ 1.75 GHz) when compared to the simulated results. This is due to one obvious issue. The low dielectric section widths were not the same as the designed widths. The accuracy of the center frequency is lackluster, yet the reflective aspect of this design was achieved. The experiment can be replicated to achieve a better center frequency.

3.2 Chebyshev Antireflective Structure

As a second example, I designed and fabricated an integrated antireflective structure for guided waves. The structure is composed of multiple quarter wavelength sections that are gradually varied to match impedance from a low permittivity substrate to a high permittivity region (illustrated in Figure 3.6). By properly selecting the dielectric properties of the matching layers, one can achieve relatively low reflectance over a broad frequency band.

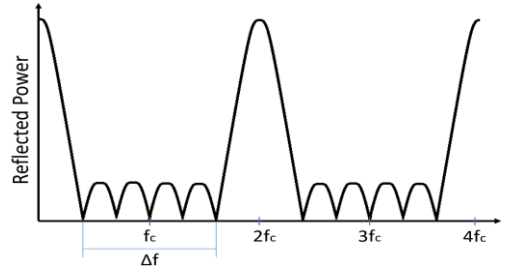


Figure 3.5: Antireflective structure response

3.2.1 Simulations and Design

As a baseline structure, I first fabricated the transmission line shown in Figure 3.7. Here the powder printer was used to create a high permittivity region, 112 mm in length, without any impedance matching layers. For this example, the high permittivity region had a dielectric constant of $\epsilon_{\text{high}}=6.5$ compared to the permittivity of the unprinted region ($\epsilon_{\text{low}}=4.3$). This large impedance mismatch results in a frequency dependent reflection coefficient as illustrated by the standing wave pattern of Figure 3.8. To design the impedance matching layers needed to minimize these reflections, I employed Collin's [17] method based on Chebyshev polynomials. For this example, a center frequency of 1.5 GHz was selected so that the quarter

wavelength sections were of reasonable length (i.e. > 25 mm). Through computational experimentation, I found that three dielectric sections was enough to significantly reduce reflection over a relatively large wide bandwidth. Using these parameters of Collin's method resulted in the three impedance matching layers described in Table 3.2.

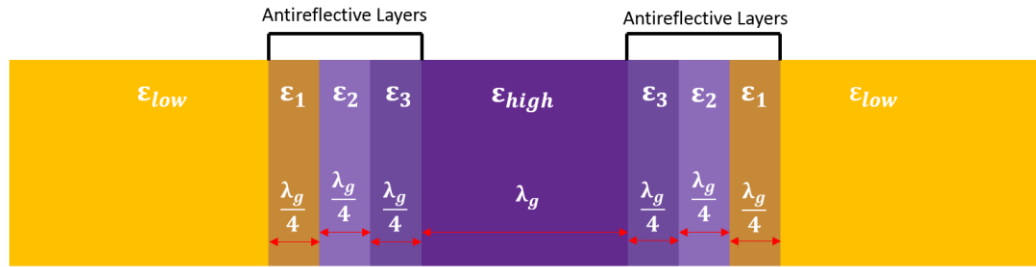


Figure 3.6: Antireflective template

Table 3.2: Antireflective structure parameters

Layer #	Relative Permittivity	Section Length (mm)
1	4.5	27.5
2	5.3	26.0
3	6.2	22.5

3.2.2 Results

The final fabricated sample, including all of the antireflective layers described in Table 3.2, is shown in Figure 3.7. Here, two microstrip lines were included to investigate any lateral variation in the printed material properties.

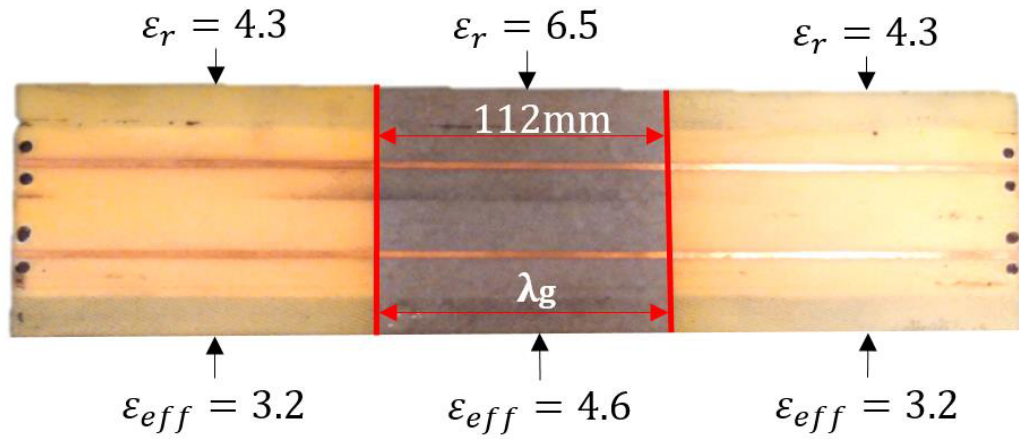


Figure 3.7: Fabricated baseline transmission lines

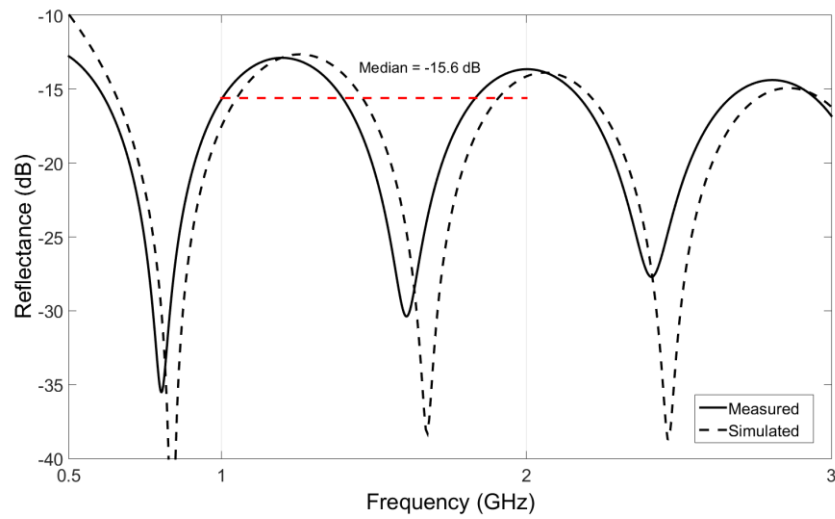


Figure 3.8: Fabricated baseline reflection response

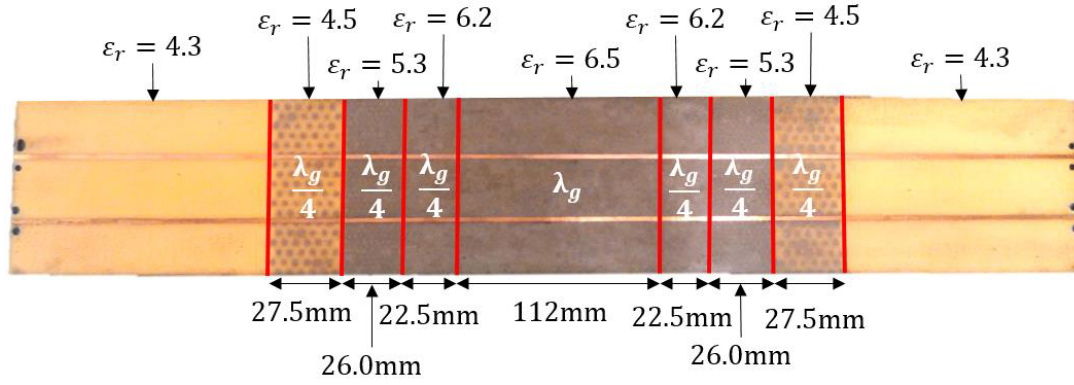


Figure 3.9: Fabricated antireflective transmission line

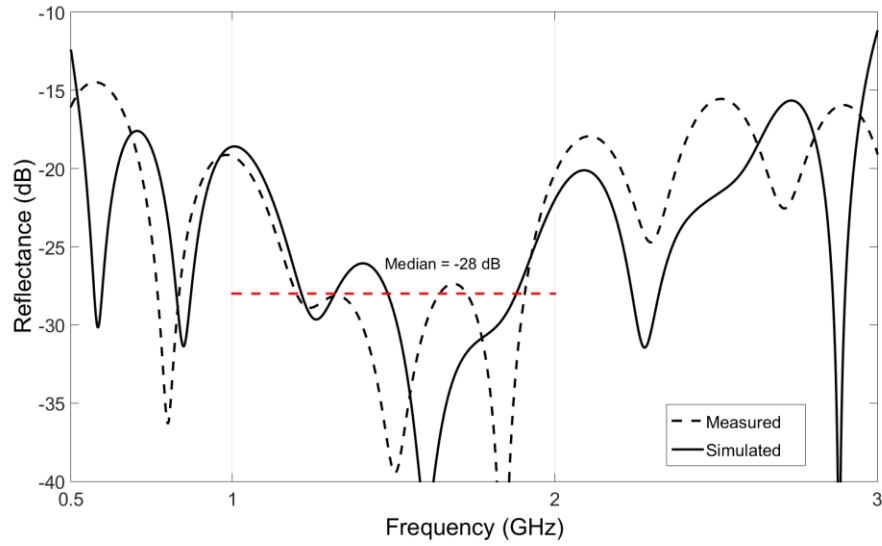


Figure 3.10: Fabricated antireflective reflection response

The reflectance was measured from 0.5 GHz to 3 GHz as shown in Figure 3.10. Also shown in the figure are predicted results using HFSS [20]. Between 1.0 GHz and 2.0 GHz, the measured reflectance had a median value of -28 dB. Compared to the baseline sample I achieved a 12 dB reduction in reflectance as a result of the antireflective layers.

3.3 Cylindrical Luneburg Lens

The Chebyshev antireflective design is an example of the increasingly complex systems the machine is capable of manufacturing since the design utilizes five locations found on the calibration curve. In contrast, the Bragg reflector utilizes two points on the calibration curve. The next logical step is to create a system that utilizes a much more complex dielectric gradient.

The Luneburg lens is a very popular design in academic journals. It is an excellent demonstration of being able to tailor one or multiple materials to create a gradual dielectric distribution. A Luneburg lens is capable of beamforming. This works by accepting a spherical point source at the input of the lens and outputting a plane wave (Figure 3.11).

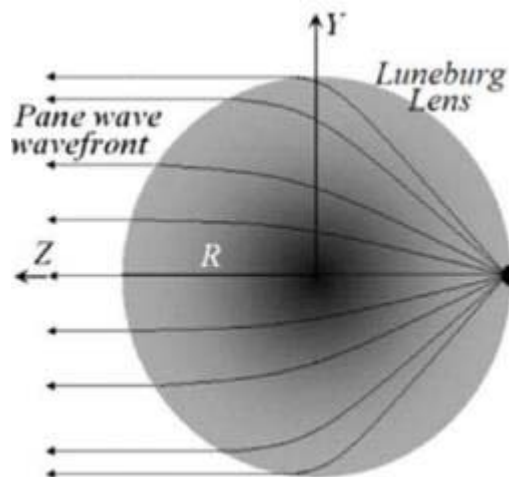


Figure 3.11: Luneburg lens excitation and output [19]

The output/input relationship is reciprocating. Accepting a plane wave as an input will converge to single point at the output.

Beamforming is a very popular technique in communications. Beamforming provides directionality and constructive/destructive interference for a propagating signal. There are two forms of beamforming approaches: active and passive beamforming. Active beamforming utilizes signal-processing algorithms to constructively add phases of desired signals. Active beamforming systems tend to be very expensive. Passive beamforming systems, on the other hand, are significantly cheaper. GRIN passive beamforming systems utilizes phase delay and refraction to provide directionality. Propagating signals travel slower in a higher dielectric medium. This concept is utilized to produce desired phase delays.

The printing process is limited in the sense that one cannot 3D print spherical Luneburg lenses. Fortunately, a cylindrical Luneburg lens can be fabricated. A cylindrical Luneburg lens lacks one dimension compared to the spherical. The output of a spherical Luneburg lens delivers a propagating plane wave that is consistent across two dimensions (plane wave). Therefore, a cylindrical Luneburg lens will deliver a propagating vector that is consistent across one dimension. The simulations and design section (3.3.1) will explore the relative permittivity distribution used for the lens and how it will be implemented to create a cylindrical Luneburg lens.

3.3.1 Simulations and Design

The traditional Luneburg lens distribution starts at an index of refraction $\sqrt{2}$ and radially decays to 1 (see Equation 6).

$$n = \sqrt{2 - \left(\frac{r}{R}\right)^2} \quad (6)$$

The powder printer characterization curve takes a prescription of relative dielectric constants (not indices of refraction). Therefore, the dielectric constant

gradient will be backed out from the index of refractive gradient by squaring the equation (6).

$$n = \sqrt{\mu_r \epsilon_r} \quad (7)$$

$$\epsilon_r = 2 - \left(\frac{r}{R}\right)^2 \quad (8)$$

Figure 3.12 shows the traditional dielectric constant distribution for a Luneburg lens.

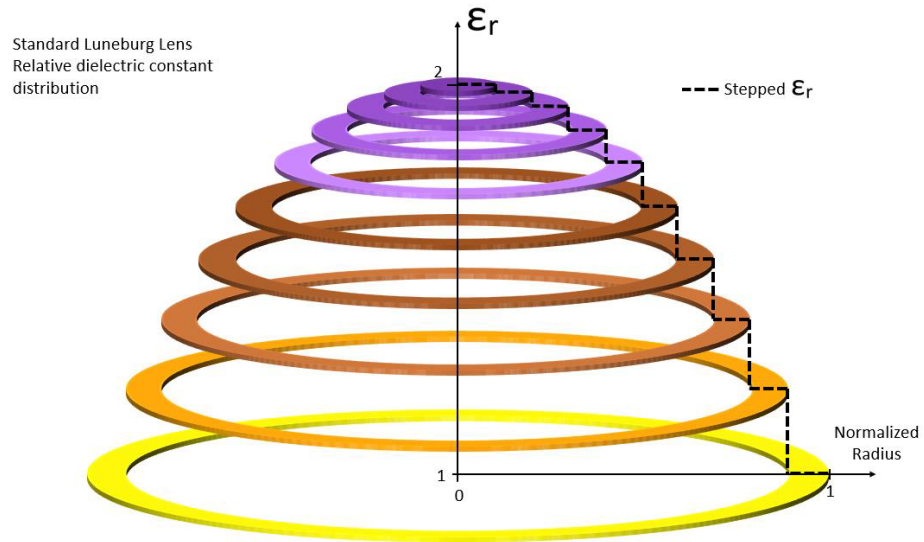


Figure 3.12: Standard Luneburg lens dielectric constant distribution

Unfortunately, the combination of materials will not permit us to produce an effective dielectric constant anywhere between 1 and 2. Therefore, the dielectric constant distribution will be scaled up by a factor of 4.3 in order to achieve a dielectric constant range that the printer can actually produce (equation 9).

$$\epsilon_r = 4.3 * \left(2 - \left(\frac{r}{R}\right)^2\right) \quad (9)$$

This produces a dielectric constant range starting at 8.6 and ending at 4.3. This range of relative permittivities are present on the in-plane calibration curve. Figure 3.13 demonstrates the scaled Luneburg lens dielectric constant distribution.

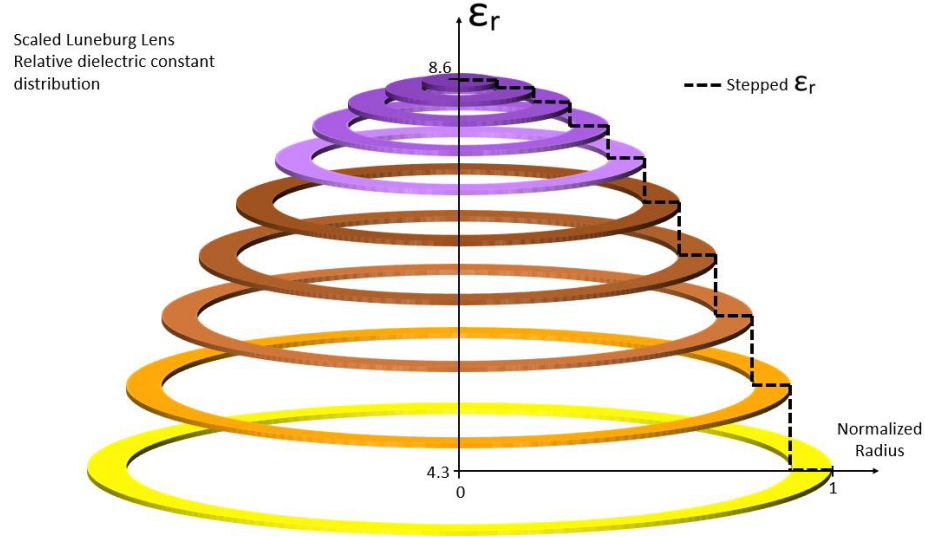


Figure 3.13: Scaled Luneburg lens relative dielectric constant distribution

High Frequency Structural Simulator (HFSS) [20] was utilized to examine if this scaled distribution would be effective in a cylindrical passive beamforming network. Unfortunately, this produces an output phase front that was not ideally flat. Several variations of dielectric constant gradients were tested in order to find a distribution that yields a very flat phase front at the output. Figure 3.14 shows the optimized dielectric distribution utilized in the constructed lens.

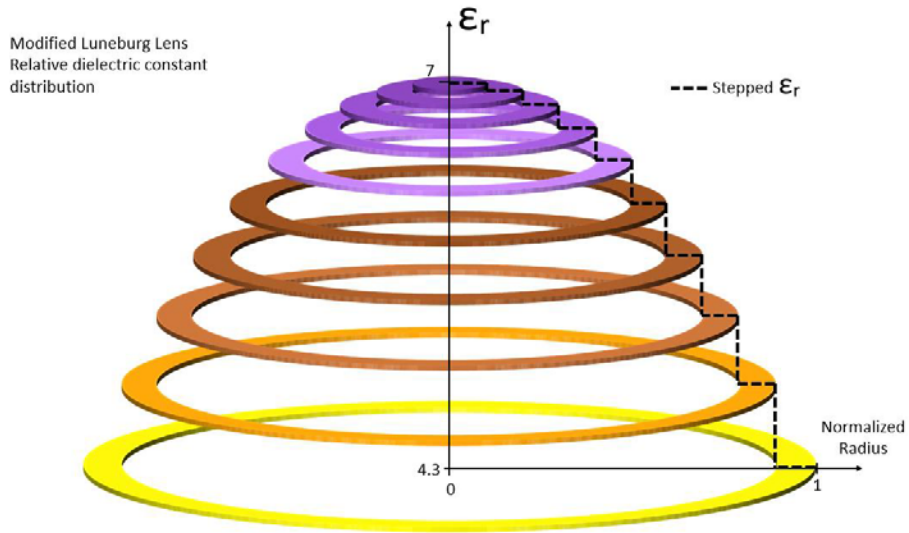


Figure 3.14: Modified Luneburg lens relative dielectric constant distribution

This dielectric constant distribution will be utilized in constructing a model in HFSS that will be connectorized and tweaked for optimal performance. Figure 3.15 is the final HFSS model. This HFSS model will be the blueprints for the constructed cylindrical Luneburg lens. This model was inspired by a combination of multiple academic journals: [19] and [21-25].

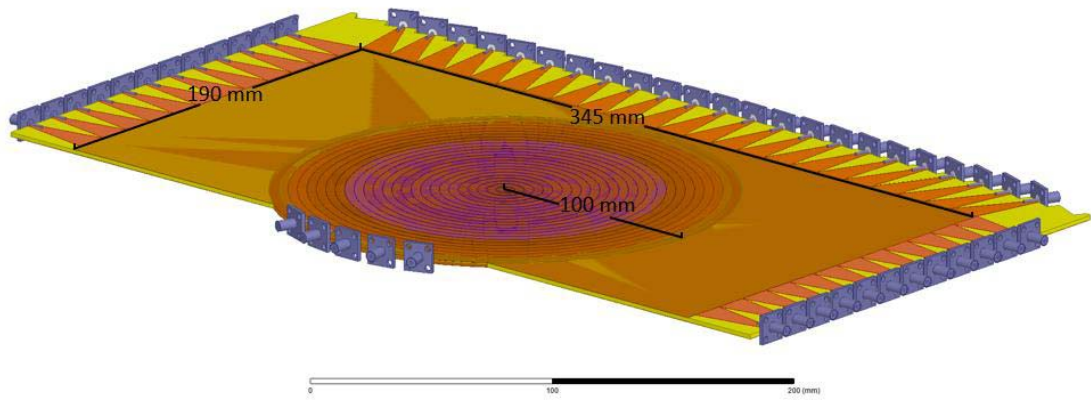


Figure 3.15: HFSS model of cylindrical Luneburg lens

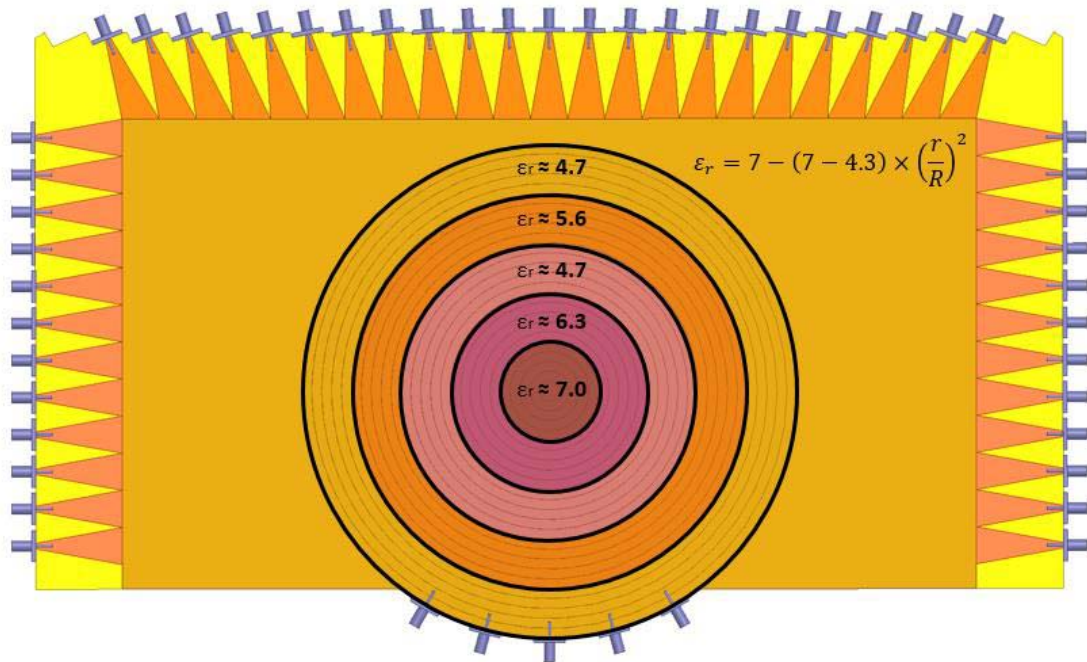


Figure 3.16: HFSS model of cylindrical Luneburg lens with annotated dielectric distribution

The constructed passive beamforming network is modeled in Figures 3.15 and 3.16. The lens is excited with a SMA connector [26]. The excitation delivers a circular phase front. The dielectric gradient then gradually transforms the circular phase front to a flat phase front at the output of the gradient. The propagating fields transition into an array of microstrip outputs. The microstrip transmission lines terminate at SMA connectors. Figure 3.17 shows how the system will operate without a dielectric gradient.

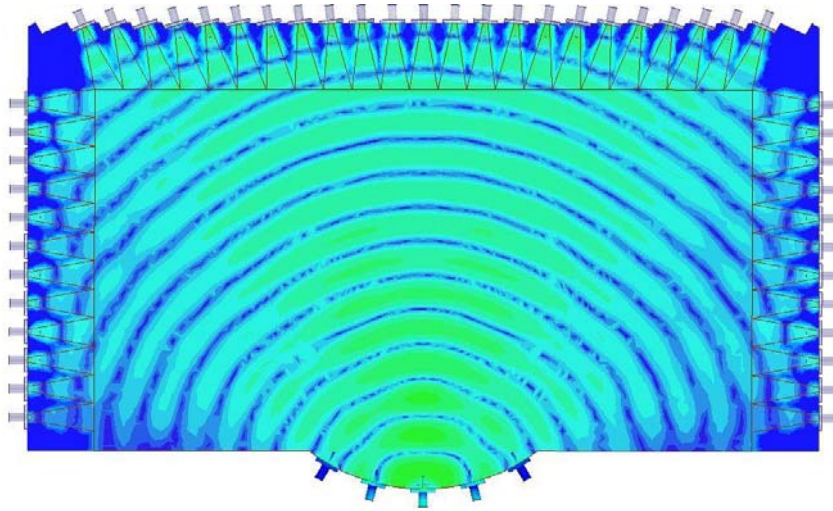


Figure 3.17: System without dielectric gradient

In order to deliver a flat phase front at the microstrip outputs, a dielectric gradient is utilized. Once the optimized gradient is applied to the center of the substrate, as shown in Figure 3.16, the system will be capable of beamsteering. Figures 3.18 through 3.27 demonstrate the effectiveness of the dielectric distribution at various input offsets.

Two different figures are used to show the results of the HFSS model: 2D heat map of the electric fields and the unwrapped phase at the output interface. There are two of these figures for five different configurations: -30 degree, -15 degree, 0 degree, +15 degree, and +30 degree input offsets. The results are on the next five pages.

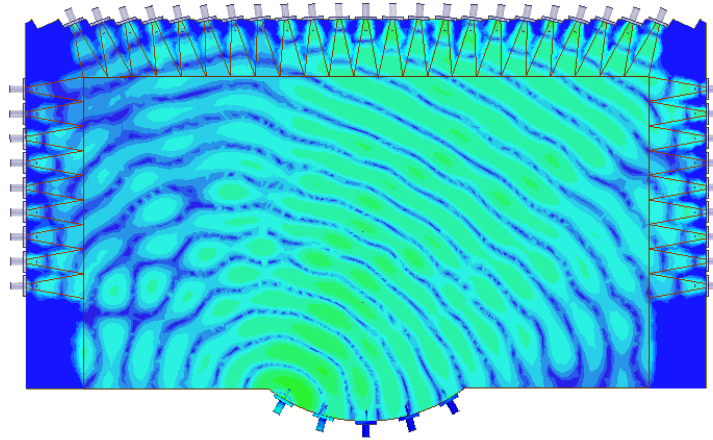


Figure 3.18: Electric field color map of -30 degree input

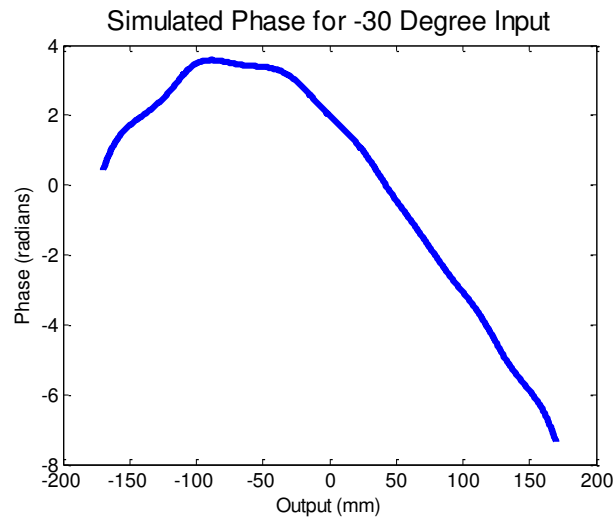


Figure 3.19: Unwrapped normalized phase using the -30 degree input

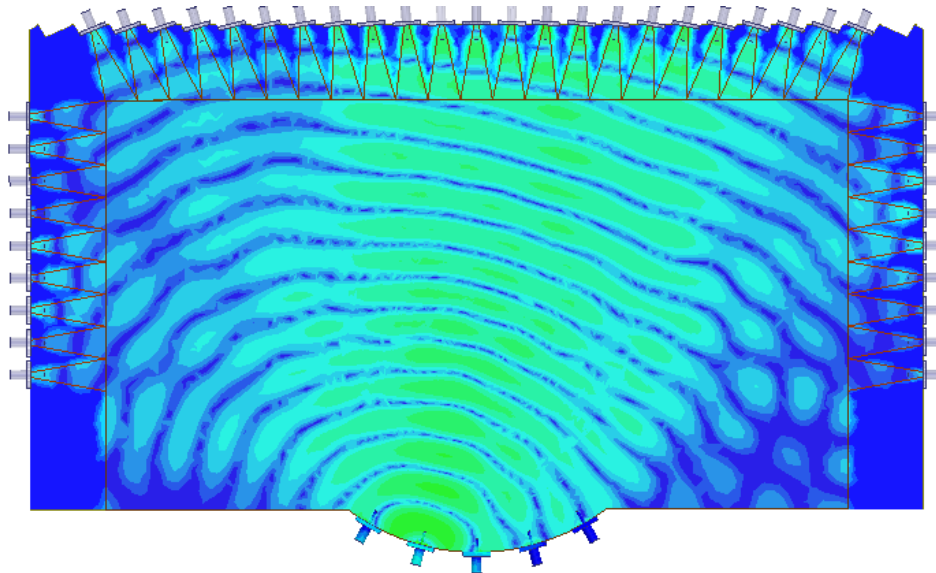


Figure 3.20: Electric field color map of -15 degree input

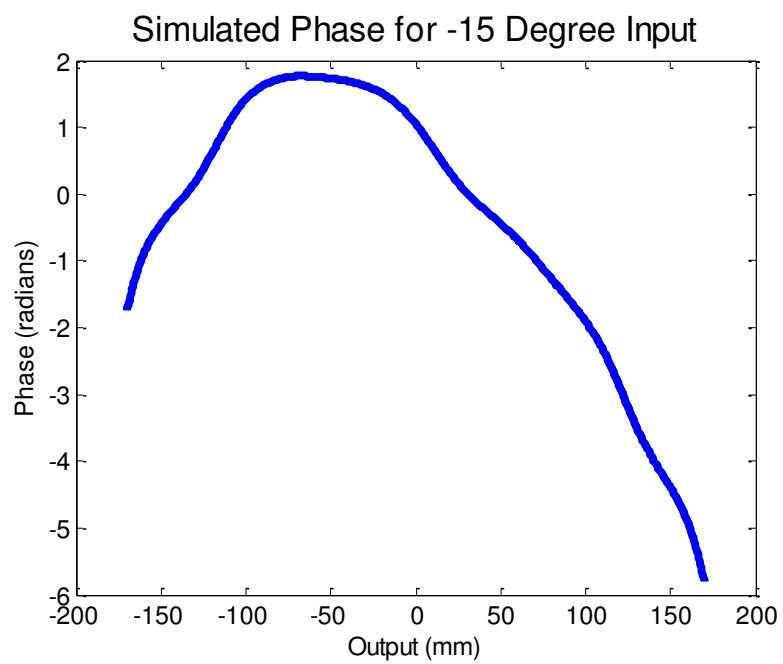


Figure 3.21: Normalized unwrapped phase using the -15 degree input

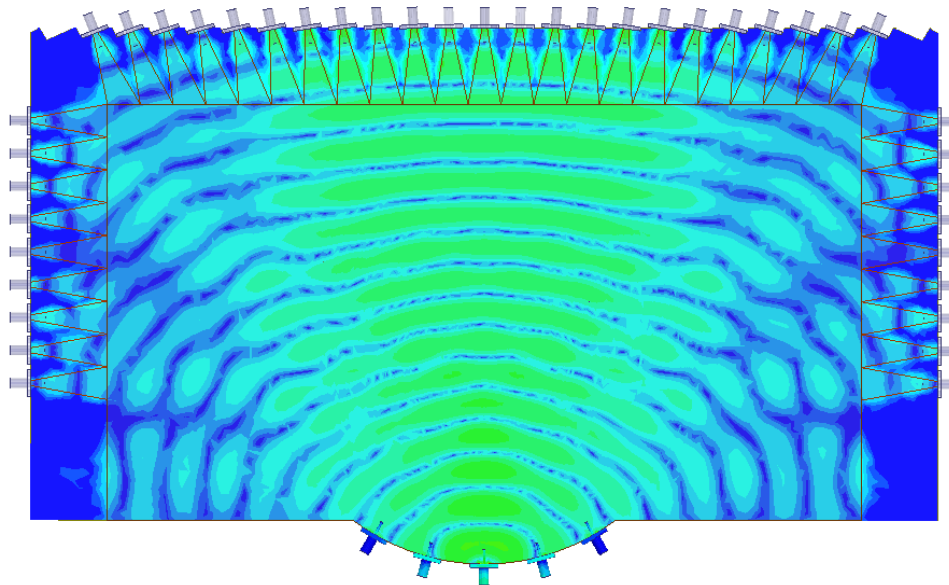


Figure 3.22: Electric field color map of 0 degree input

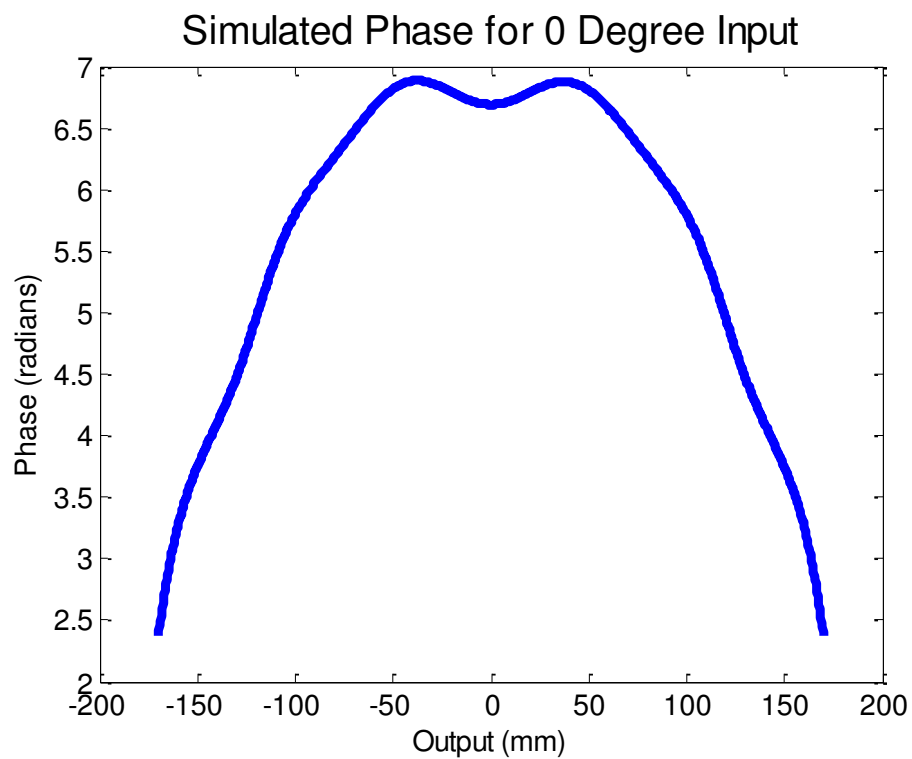


Figure 3.23: Normalized unwrapped phase using the 0 degree input

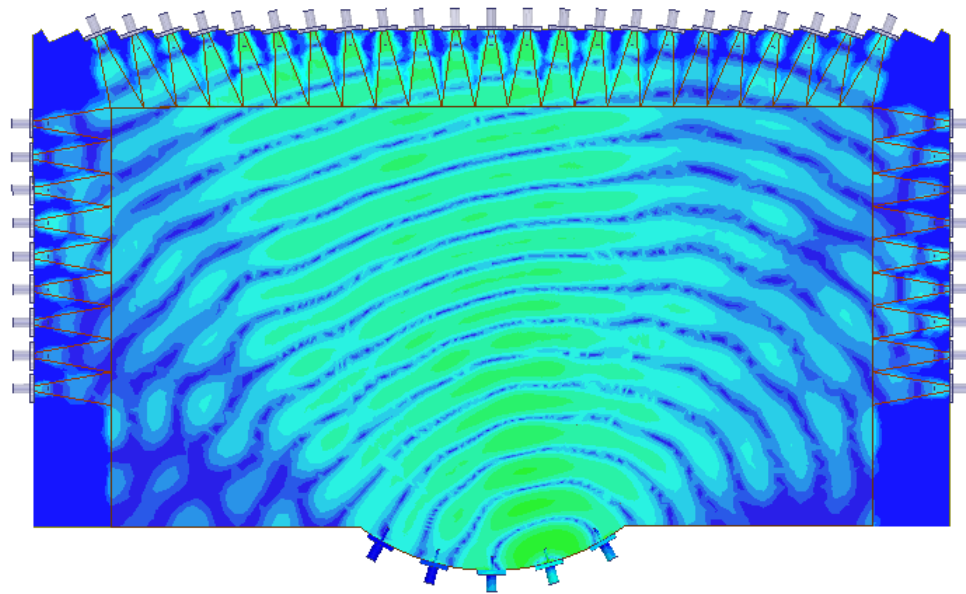


Figure 3.24: Electric field color map of +15 degree input

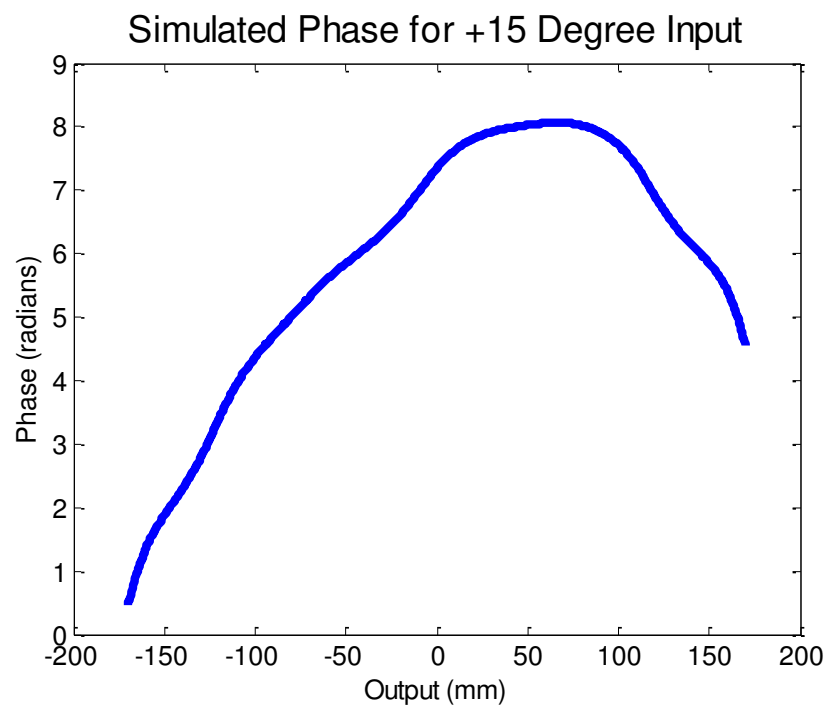


Figure 3.25: Normalized unwrapped phase using the +15 degree input

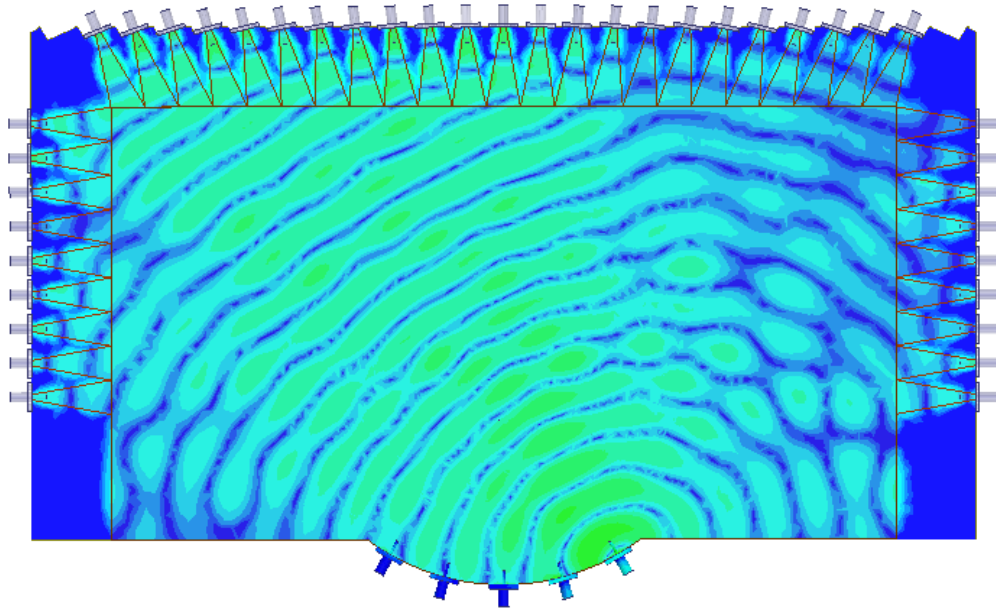


Figure 3.26: Electric Field color map of +30 degree input

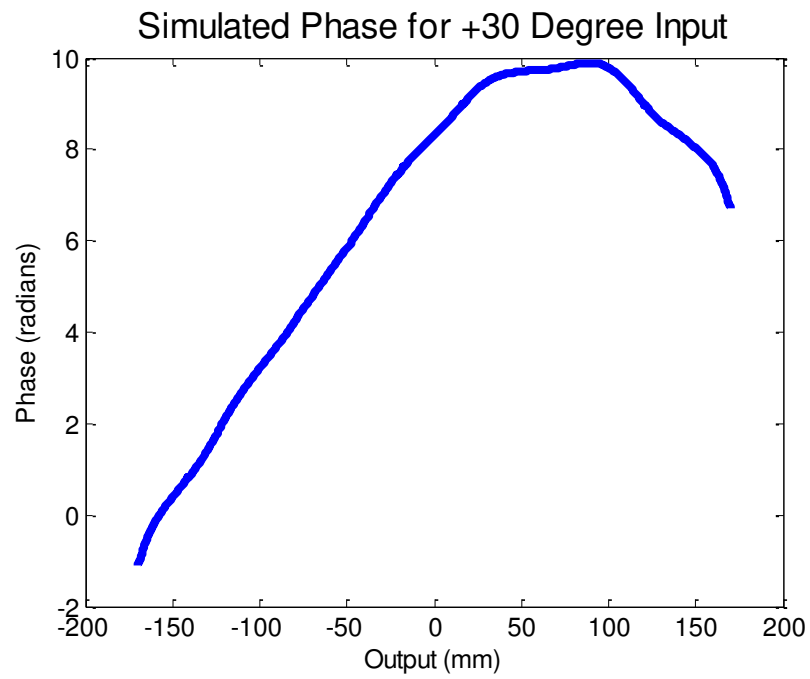


Figure 3.27: Normalized unwrapped phase using the +30 degree input

The simulated results are promising. The passive beamforming network will be effective if the permittivity distribution can be replicated in the fabricated substrate. Chapter 3.3.2 will explain the fabrication process and Figure 3.33 shows the fabricated substrate containing the lens.

3.3.2 Fabrication of Cylindrical Lens

Unlike the last two designs, the cylindrical lens requires a finer graded dielectric constant distribution. I did this by creating a MATLAB script that would generate concentric rings of dots. As the distance from the center of the circle increases, the dots would separate themselves more and the space between rings would increase. By utilizing the in-plane characterization curve, I was able to figure out the dot spacing found in each of the rings as well as the radial spacing of the rings. Figure 3.28 shows the MATLAB generated figure that is exported to the printer.

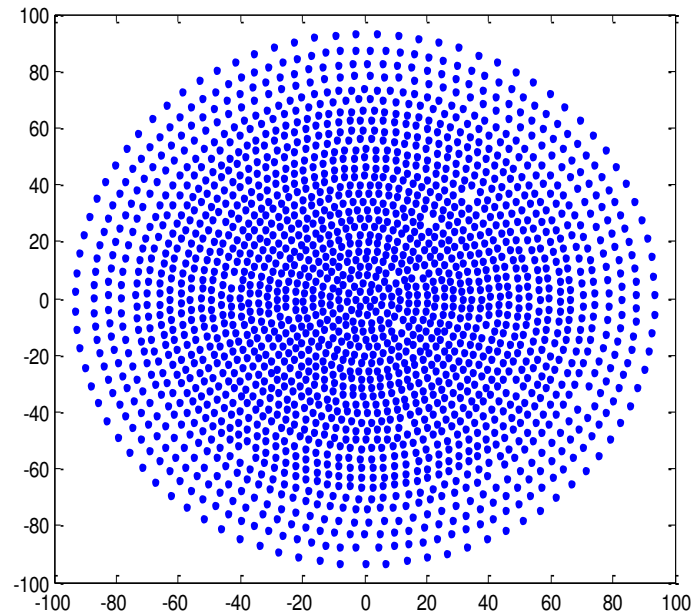


Figure 3.28: MATLAB figure of dot distribution exported to the 3D powder printer

This dot pattern was dispensed on prepreg 4 times between 5 layers. In order to replicate the model created in HFSS, portions of the substrate needs to be removed. The substrate is placed in a water jet cutter to remove unwanted sections of prepreg. Figure 3.29 shows the substrate before water jet cutting. Figure 3.30 shows the substrate after water jet cutting. A copper ground plane is also cut in the water jet cutter (Figure 3.31).

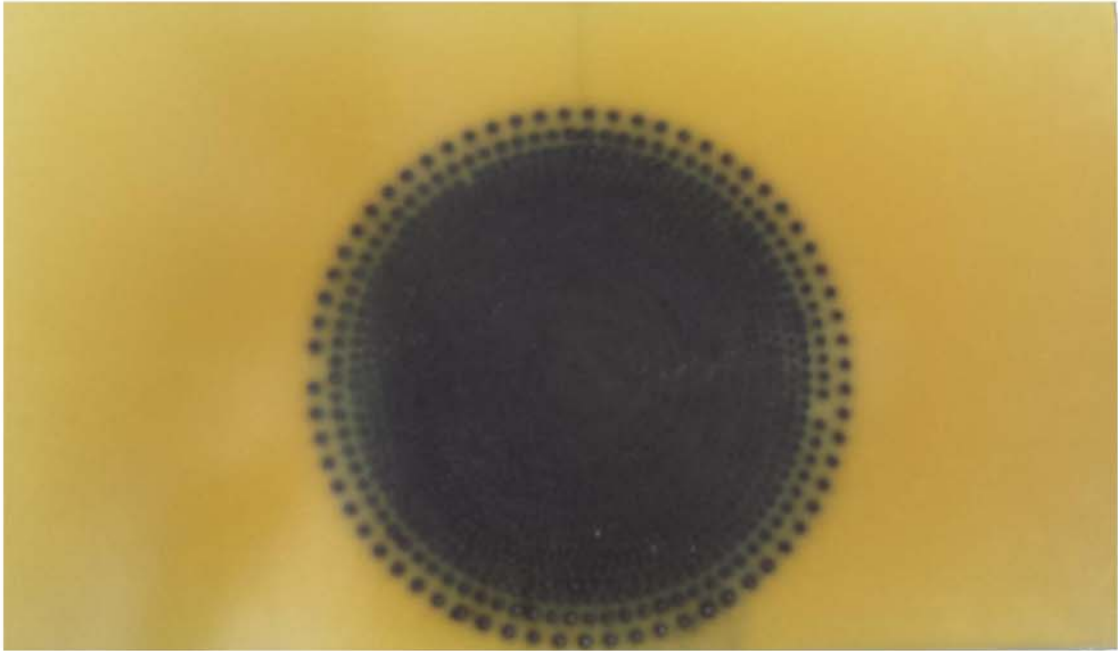


Figure 3.29: Printed substrate

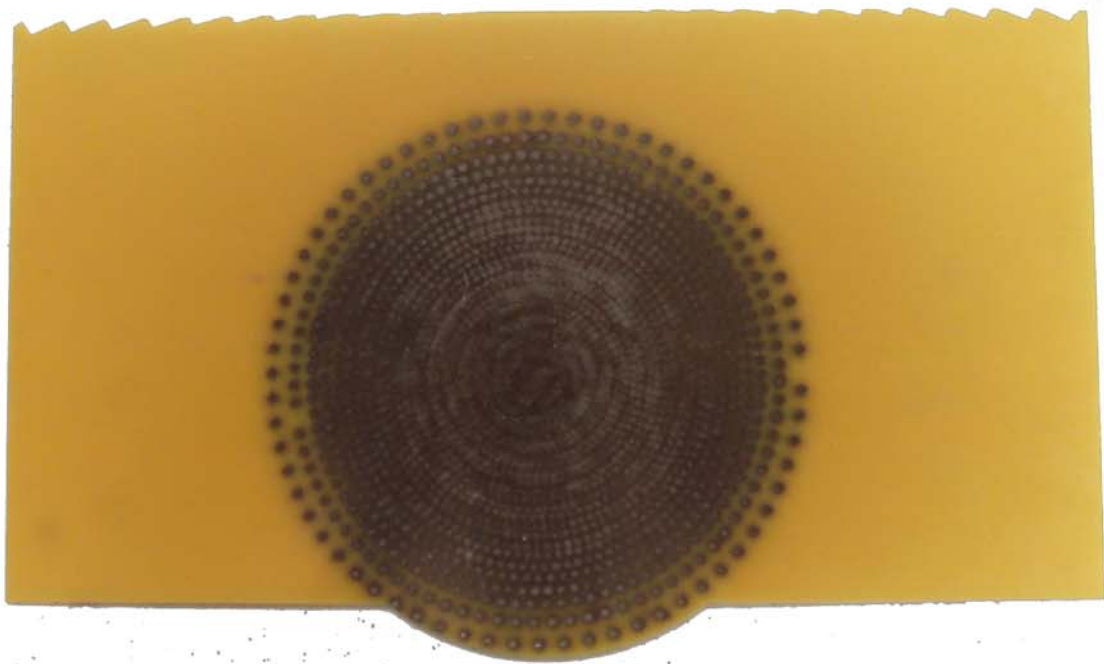


Figure 3.30: Printed and cut substrate

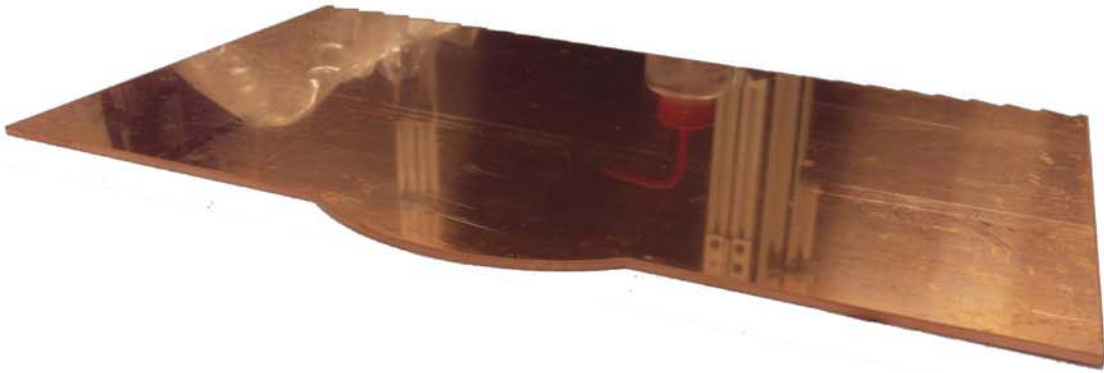


Figure 3.31: Cut ground plane

After cutting the substrate, the top conductor and ground plane need to be attached. The top conductor is attached by using a conductive adhesive to bind a thin copper foil to the substrate. The microstrip patterns are created through copper etching. This is done by first spray-painting the copper foil with a black spray paint containing a protective enamel. To expose the copper to be etched, a laser cutter is used to expose copper that is to be etched. The laser cutter used the follow CAD file (Figure 3.32) to lase the black spray paint. The black portions of Figure 3.32 are where the laser cutter will burn the spray paint.

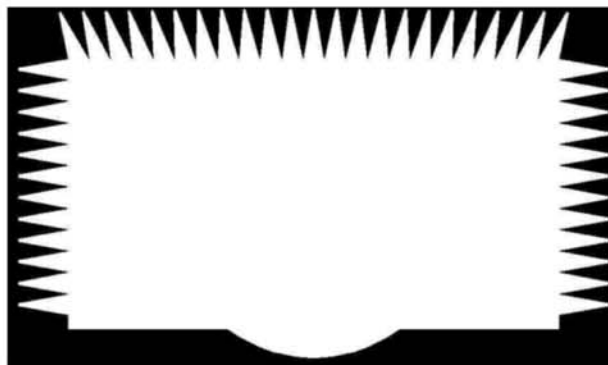


Figure 3.32: CAD file used for patterning top conductor

After lasing, the exposed copper is etched away using a FeCl solution. Next, the ¼” thick ground plane Figure 3.31 is adhered to the bottom of the substrate. After the ground plane is attached, coaxial connectors are attached to the top conductor and ground plane. This is done by drilling holes on the side of the ¼” ground plane for the coaxial connectors to be connected. The SMA connectors (Figure 3.33) have 4 ground vias. One 1-72 screw is attached to the ground plane through one ground via of the connector. The completed part is shown in Figure 3.35.



Figure 3.33: SMA connector and terminating load (images acquired from Digi-Key [26-27])

The purpose of the SMA connectors is to excite the input interface of the lens and to capture the energy at the output interface. The SMA connectors (ACX1827-ND) have a 50 Ω impedance. In order to minimize reflections at the output interface, the microstrip outputs are tailored to have a 50 Ω impedance as well.

In order to measure this part without dummy loads, we would need to use a 20+ port network analyzer. Since we only have a 2 port network analyzer, dummy 50 Ω loads are attached to all the outputs excluding the output that is being measured.

The dummy loads are shown in figures 3.33 (by itself) and 3.34 (attached to the final part). The results of the completed part are found in the next section.

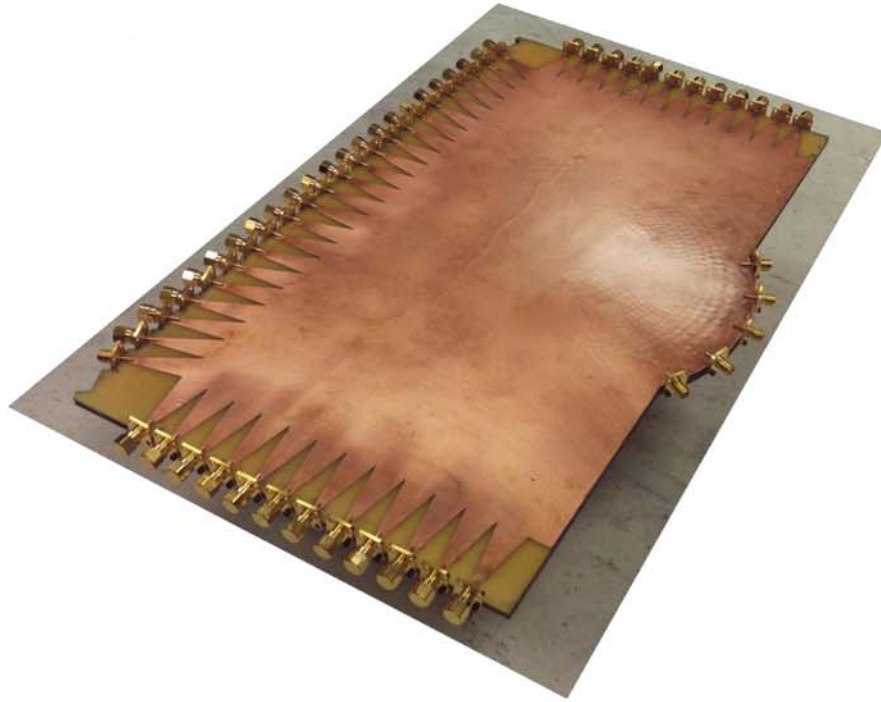


Figure 3.34: Fabricated part

3.3.3 Results

To begin, we need to get an impression as to how well the power actually makes it into the fabricated part. This can be done by studying the return loss and insertion loss across a range of frequencies at the center input. To take this measurement, all output ports have dummy loads attached to them except the center output port. The 1-port is attached to 0 degree input SMA, and the 2-port is attached to the center output SMA. The results are depicted in Figures 3.35 (S11) and 3.36 (S21).

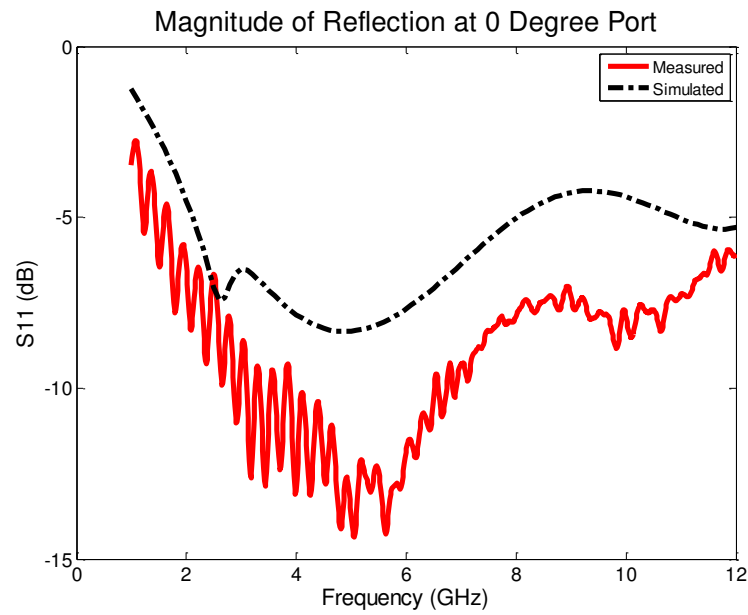


Figure 3.35: Reflection

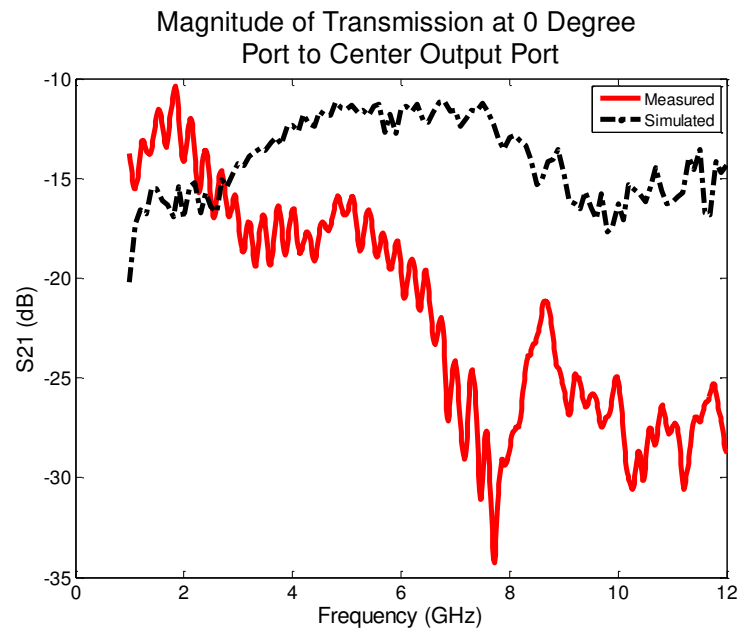


Figure 3.36: Transmission

Traditionally, a return loss below -10 dB suggests a sufficient amount of power entering a system. Therefore, 2-7 GHz seems attractive with only this bit of information. However, we need to examine S21 before selecting a frequency to extract the unwrapped phases at the outputs. Figure 3.36 shows the best performance between the frequencies 1 GHz and 2 GHz. By combining the information provided by S11 and S21, 2 GHz is selected for extrapolating the unwrapped phases at the output interface.

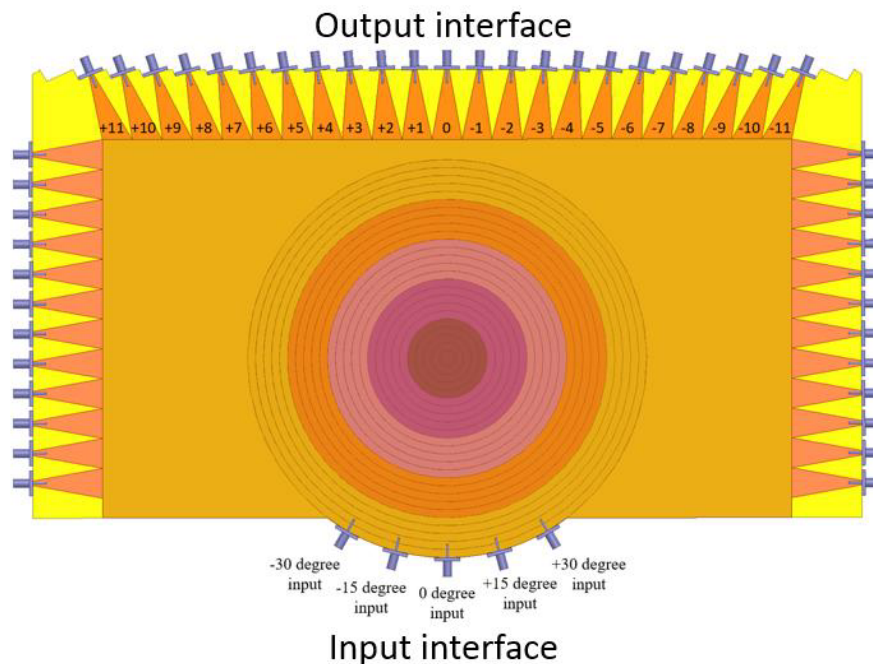


Figure 3.37: Input/output configuration for measurements

The next step is to measure the many combinations of input and output ports using the network analyzer. Figure 3.37 will be referenced while describing the measuring process. The measuring process starts by terminating all side and output microstrips, excluding output +11, using the dummy loads described earlier. The input

ports do not have dummy loads attached. To start the measuring process, attach port 1 of the network analyzer to the -30 degree input and port 2 to the +11 SMA connector. The next step is to save the frequency sweep between 1 and 12 GHz. Once the data is saved, remove the dummy port from +10 and attach port 2 of the network analyzer to output +10. Take the dummy port you removed from output +10 and place it on +11. Repeat this process until all measurements have been taken up to -11 output. This is all the data for the -30 degree input. The next steps are to repeat the previous steps for the -15, 0, +15, and +30 degree inputs. Once the process is complete, you should have a total of 115 saved .cti files on the network analyzer. This data will be post-processed in MATLAB to generate plots to demonstrate the effectiveness of the lens. The results are demonstrated in Figures 3.38 through 3.42.

Ideally, the results should follow the simulated results in the previous section. The simulated and measured results are plotted on the same figure for comparison. After examining the unwrapped phase results, the results follow the simulated trends found in HFSS.

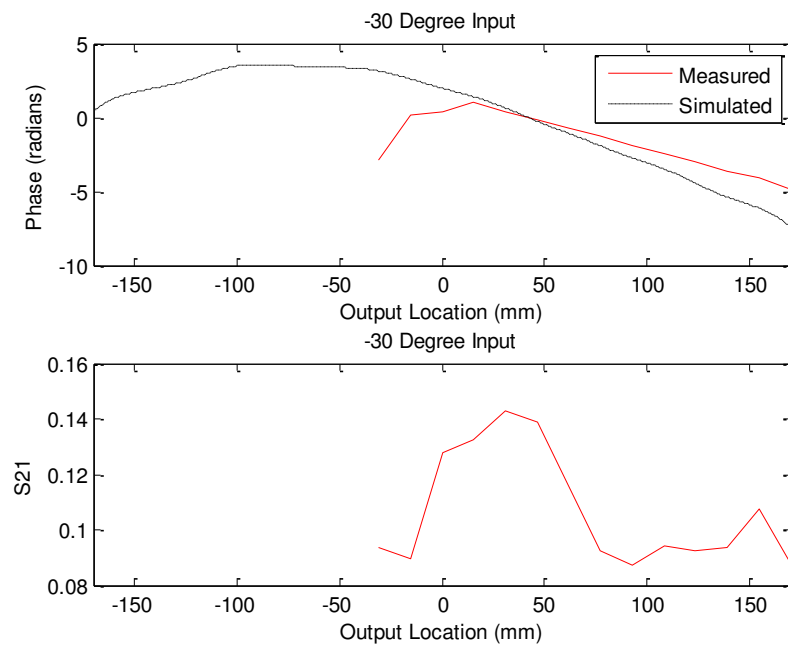


Figure 3.38: -30 degree input

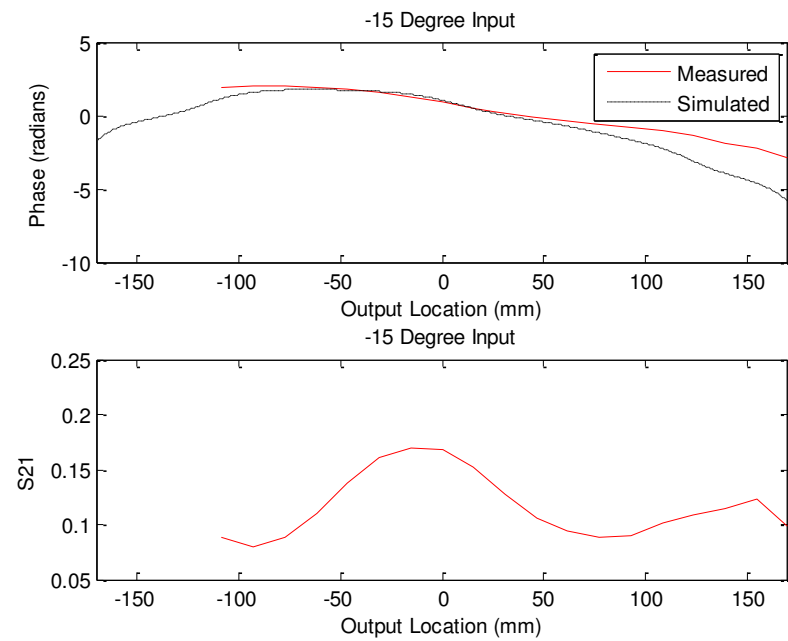


Figure 3.39: -15 degree input

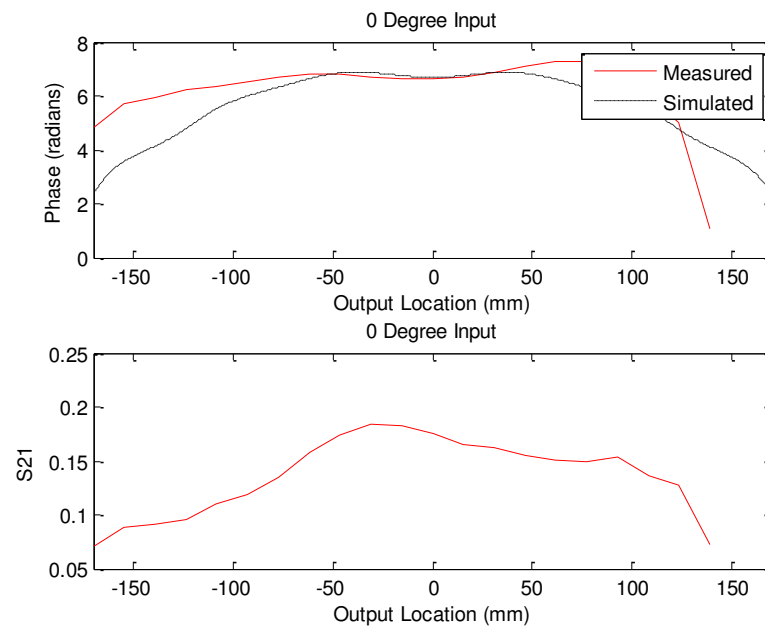


Figure 3.40: 0 degree input

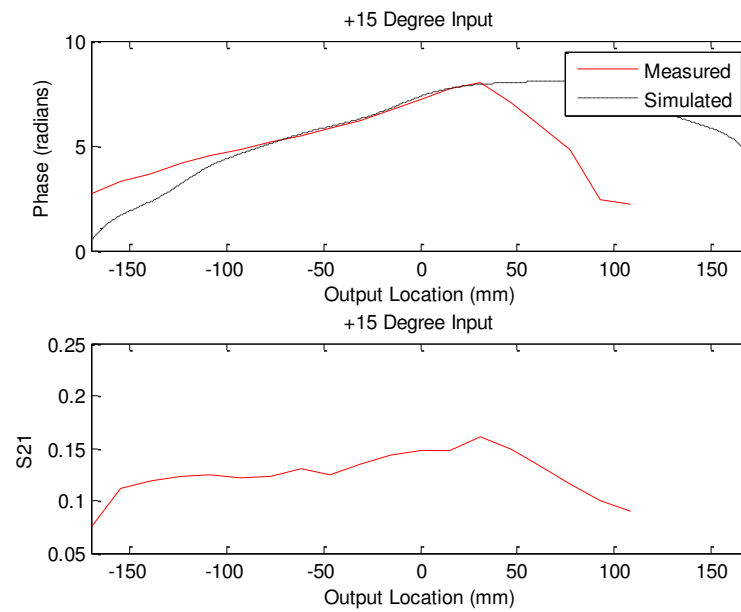


Figure 3.41: +15 degree input

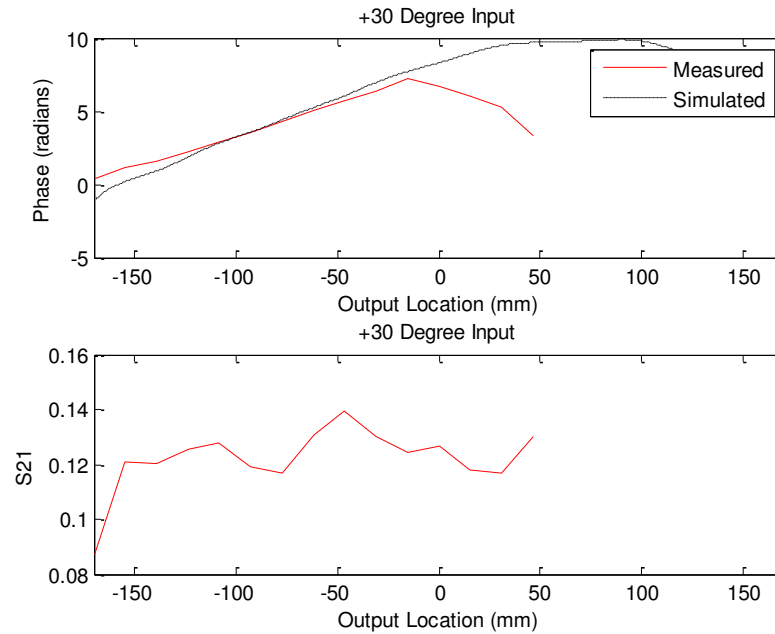


Figure 3.42: +30 degree input

The results show that the printed cylindrical lens is performing the fundamental concept of a beamsteering network. As you sweep the input locations, the flat phase front found at the output is changing its orientation. The best explanation I can provide for the minor discrepancies between the simulated and measured is a fabrication error that occurred during the water jet cutting process. Looking closely at the bottom of Figure 3.30, it is apparent that the cut is not centered at the base of the substrate. In fact, the cut was shifted to the right approximately 1 cm. This offset can cause the results to “lean” left. This is the most apparent in the 0 degree, -15 degree, and -30 degree input angles. In the 0 degree input unwrapped phase results, the flat phase front does not appear to be steered at 0 degrees. It is slightly steered to the left. Other measurements also show the same behavior. Since this error is consistent across

all the measurements, the fabrication error described earlier explains the discrepancy between the measured and simulated results.

Chapter 4

CONCLUSION

4.1 Summary of Work

This thesis demonstrates the capabilities of the 3D powder printer. The powder printer is capable of integrating a high dielectric constant ceramic powder between layers of preimpregnated S-glass composite. The ability to dispense a high dielectric powder in a low loss substrate allows the user to spatially vary the dielectric constant of a robust structure. Through these means, electromagnetic systems can be incorporated into a mechanical structure. In order to build these electromagnetic systems, the combination of preimpregnated S-glass and dry ceramic powder must be characterized in terms of powder density and effective permittivity. This was achieved by creating an effective permittivity calibration curve that is determined by local powder density (mg/mm^2). The calibration curves capture the anisotropy of the materials by plotting both the in-plane and out-of-plane effective relative permittivities. The calibration curve is then utilized to create electromagnetic systems within the described structural composite. The effectiveness of these systems will verify the accuracy of the calibration curve.

The first electromagnetic system, Bragg dielectric reflector, was the simplest in complexity. The Bragg dielectric reflector consists of multiple high and low dielectric sections. This results in high reflectivity at the designed center frequency. This substrate was used to fabricate a microstrip transmission line. There was one

fabrication error that yielded in a slightly shifted center frequency, but the high reflectivity was achieved.

The second electromagnetic system fabricated increases in complexity. The complexity increases by utilizing five points, instead of two, on the calibration curve to create Chebyshev antireflective layers. The goal of the Chebyshev antireflective layers is to create broadband reduction in reflection caused by an impedance mismatch at a dielectric interface. The Chebyshev antireflective system was also fabricated using a microstrip transmission line. The completed antireflective system yields a median 12 dB broadband reduction in S_{11} . The Chebyshev antireflective matching system proves to be a successful method of reducing reflecting standing waves caused by an impedance mismatch.

The final electromagnetic system was by far the most complex. By utilizing several points on the calibration curve, a modified Luneburg lens or a passive beamsteering network was created. The Luneburg lens is a dielectric gradient that will provide a flat phase front at the output when excited with a spherical/circular phase front at the input. The Luneburg lens also provides directionality at the output by simply sweeping the input interface of the lens. To design a system that could achieve these characteristics, High Frequency Structure Simulator (HFSS) was used. HFSS was used to tweak parameters of the lens to achieve an optimal dielectric gradient, return loss, and insertion loss. HFSS was also used to simulate the peripherals that excite the lens and capture the power at the output of the lens. Upon building a sufficient model in HFSS, fabricating a part that mimics the HFSS model is next. The constructed part consists of a parallel plate system with the lens in the substrate and microstrip outputs to capture the output energy. After examining the similarities

between the simulated and measured results, the constructed beamsteering network operates as intended.

The three built systems described in my thesis operate as designed. The success of these systems demonstrate that 3D powder printing is a powerful technique to spatially vary the dielectric constant of a structural composite. The ability to spatially vary the permittivity of a material gives an engineer the ability to build various electromagnetic systems.

4.2 Future Work

The 3D powder printer has some limitations. First, the spatial resolution is limited by the dot size of one pulse of powder (2-2.5 mm). Secondly, the dielectric constants produced by the printer is restricted to certain ranges. For in-plane incidence, the dielectric constant ranges between 4.2 and 8.5. For out-of-plane incidence, the dielectric constant ranges between 4.2 and 10.7. Thirdly, the maximum part size is limited by the printer's platform size. Lastly, the printing process is slow and not very scalable. Fabricating a part that utilizes the 3D powder printer can take anywhere between two days to a week. nScript provides additive manufacturing systems that can overcome some limitations seen by the 3D powder printer.

nScript's 3Dn-300 [28] system has the ability to micro-dispense low to high viscosity materials at the micron scale. It also has the ability to print a wide variety of thermal plastics.



Figure 4.1: nScript's 3Dn-300 additive manufacturing system [28]

There are two limitations that are overcome by using this system when compared to 3D powder printing. These limitations are the poor spatial resolution and limited range of dielectric constants of the 3D powder printing system. The nScript has the ability to print features that are a few hundred microns in size. This reduces the spatial limitation approximately five hundredfold. Also, the materials this system can print are virtually endless. This alleviates being confined to a set range of dielectric constants.

By utilizing nScript's additive manufacturing system, one can replicate the previous electromagnetic systems described in this thesis. But, these systems can be built with more precision. Possible future work involves replicating the mechanically robust electromagnetic systems described in this thesis but utilizing the nScript's micro-dispensing/thermoplastic deposition system. Also, additional electromagnetic systems can be explored that are not listed in this thesis.

REFERENCES

1. M. Imbert, A. Papió, F. De Flaviis, L. Jofre, and J. Romeu. Design and Performance Evaluation of a Dielectric Flat Lens Antenna for Millimeter-Wave Applications. *IEEE Antennas and Wireless Propagation Letters: Vol. 14*, pp. 342-345.
2. M. Mirotznik, B. Good, P. Ransom, D. Wikner, and J. Mait. Broadband Antireflective Properties of Inverse Motheye Surfaces. *IEEE Transactions On Antennas and Propagation: Vol. 58*, no. 9, pp. 2969-2980.
3. Reinholdt, Johan. Cylindrical Luneburg Lens Antenna for Multi-Beam Small Cell Wireless Backhaul Applications. Thesis. Luleá University of Technology, 2014.
4. D. Roper, B. Good, R. McCauley, S. Yarlagadda, J. Smith, A. Good, P. Pa, and M. Mirotznik. Additive manufacturing of graded Dielectrics. *Smart Materials and Structures: Volume 23*, Issue 4.
5. "ECCOSTOCK® HiK Powder." - Emerson & Cuming Microwave Products. Web. 10 Apr. 2016. <<http://www.eccosorb.com/products-eccostock-hik-powder.htm>>.
6. "TenCate." BTCy-1 PIP. Web. 10 Apr. 2016. <<http://www.tencate.com/advancedcomposites/product-compare-tool/BTCy-1.aspx>>.
7. S. Chianrabutra, B.G. Mellor, and S. Yang. A Dry Powder Material Delivery Device for Multiple Material Additive Manufacturing. University of Southampton, UK.
8. Yang S and Evans J. Metering and dispensing of powder: the quest for new solid free forming techniques. *Powder Tech*: 178 56–72.
9. X. Lu, S. Yang, and J. Evans. Microfeeding with different ultrasonic nozzle designs. *Ultrasonics: Vol 49*, pp. 514-521.
10. S. Yang, and J. Evans. Metering and dispensing of powder. *Powder Technology: Vol 178*, issue 1, pp. 56-72.

11. X. Lu, S. Yang, and J. Evans. Dose uniformity of fine powders in ultrasonic microfeeding. *Powder Technology*: Vol. 175, pp. 63-72.
12. S. Yang, and J. Evans. Acoustic control of powder dispensing in open tubes. *Powder Technology*: Vol 139, pp. 55-60.
13. X. Lu, S. Yang, and J. Evans. Ultrasound-assisted microfeeding of fine powders. *Particuology*: Vol. 6, pp. 2-8.
14. S. Yang and J. Evans. A dry powder jet printer for dispensing and combinatorial research. *Powder Technology*: Vol. 142, pp. 219-222.
15. "HexForce® Reinforcements." *Technical Fabrics Handbook* www.hexcel.com. HEXCEL. Web. 10 Apr. 2016.
16. D. Pozar. *Microwave Engineering*. Hoboken, NJ 2005. John Wiley & Sons, Inc, 2012, pp 144.
17. S. Orfanidis. *Electromagnetic Waves and Antennas*. 2014, pp. 227-231, pp. 193-203 [Online]. Available: www.ece.rutgers.edu/~orfanidi/ewa
18. Lopetegi, Txema, Francisco Falcone, and Mario Sorolla. "Bragg Reflectors and Resonators in Microstrip Technology Based on Electromagnetic Crystal Structures". *International Journal of Infrared and Millimeter Waves*, 6 Nov. 1999. Web.
19. Mateo-Segura, Carolina, Amy Dyke, Hazel Dyke, Sajad Haq, and Yang Hao. "Flat Luneburg Lens via Transformation Optics for Directive Antenna Applications." *IEEE Trans. Antennas Propagat.* *IEEE Transactions on Antennas and Propagation* 62.4 (2014): 1945-953. Web.
20. ANSYS®, Inc., 275 Technology Drive Canonsburg, PA 15317, USA, *An Introduction to HFSS: Fundamental Principles, Concepts, and Use*, 2013.
21. Bor, Jonathan, Olivier Lafond, Herve Merlet, Philippe Le Bars, and Mohamed Himdi. "Foam Based Luneburg Lens Antenna At 60 Ghz." *PIER Letters Progress In Electromagnetics Research Letters* 44 (2014): 1-7. Web.
22. Sato, Kenichi, and Hiroshi Ujiie. "A Plate Luneberg Lens with the Permittivity Distribution Controlled by Hole Density." *Electronics and Communications in Japan (Part I: Communications)* *Electron. Comm. Jpn.* Pt. I 85.9 (2002): 1-12. Web.

23. Hua, Changzhou, Xidong Wu, Nan Yang, and Wen Wu. "Air-Filled Parallel-Plate Cylindrical Modified Luneberg Lens Antenna for Multiple-Beam Scanning at Millimeter-Wave Frequencies." *IEEE Transactions on Microwave Theory and Techniques* IEEE Trans. Microwave Theory Techn. 61.1 (2013): 436-43. Web.
24. Liang, Min, Wei-Ren Ng, Kihun Chang, Michael E. Gehm, and Hao Xin. "An X-band Luneburg Lens Antenna Fabricated by Rapid Prototyping Technology." 2011 IEEE MTT-S International Microwave Symposium (2011): n. pag. Web.
25. Peeler and Archer. "A Two-Dimensional Microwave Luneberg Lens" (2012. Web.
26. "ACX1827-ND." Digikey. Web. <<http://www.digikey.com/product-detail/en/amphenol-rf-division/132204/ACX1827-ND/2627841>>.
27. "ACX1251-ND." Digikey. Web. <<http://www.digikey.com/product-detail/en/amphenol-rf-division/132360/ACX1251-ND/1011928>>.
28. nScript, Inc., nScript, Inc., 2015. [Online]. Available: nscript.com. [Accessed 2016].